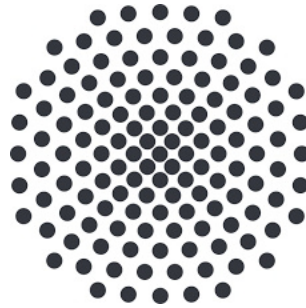# University of Stuttgart
Faculty of Aerospace Engineering and Geodesy

Master's thesis

Development of a Photogrammetry Method to Digitize Ice Shapes on UAVs

Submitted by Samuel Göhring
Stuttgart/ Trondheim, April 2024

Norwegian University of Science and Technology
UAV Icing Lab
Department of Engineering Cybernetics

Supervisor: Dr. Richard Hann
M.Sc. Nicolas Müller

University of Stuttgart
Institute of Aircraft Design

Supervisor: Dr.-Ing. Jan Pfaff

IFB Institut für Flugzeugbau · Universität Stuttgart

Master Thesis

Herrn Samuel Göhring
Riedbachstr. 3
88512 Mengen

Matrikelnummer: 3610468

Mobile: +49 152 27351011

E-Mail: samuel.goehring@outlook.de

Topic:

Development of a photogrammetry method to digitize ice shapes on UAV

Problem description:

A key limitation to the operational envelope of unmanned aerial vehicles (UAVs) today is the risk of atmospheric in-flight icing. In contrast to icing in manned aviation, UAV icing is not well established and is an emerging research topic. The NTNU UAV Icing Lab is offering a master thesis on the topic of using a photogrammetric structure-from-motion (SfM) method to digitize ice shapes.

The main objective of this project is to set up and validate a SfM process that generates 3D models based on a series of images taken of iced airfoils and rotors from icing wind tunnel experiments. The SfM method has been already tested as a proof-of-concept and this project aims to mature and develop it into a standard tool for ice shape digitization. In practice, the method consists of taking a series of pictures from different angles of iced geometries inside of a light box. The pictures are then processed with an commercial photogrammetry software (Agisoft Metashape). The main focus will be to validate that the method is generating accurate results and to generate a set of high-fidelity ice shape geometries that can be used for the validation of icing CFD simulations. The majority of the work is experimental but can also contain work packages with icing CFD simulations.

Task description:

- Literature study on aircraft icing, UAV icing, photogrammetry, and the digitization of ice shapes.
- Familiarization with the existing photogrammetry setup.
- Improvement of the photogrammetry setup with the aim to make the process repeatable.
- Generation of validation cases by scanning known ice geometries.
- Participation in an icing wind tunnel campaign where the method will be applied to wing and rotor ice shapes.
- Generate at least three high-fidelity cases to be used for icing CFD validation.
- Optional: Conduct icing CFD simulations of the high-fidelity cases with ANSYS FENSAP-ICE.
- Critical discussion of results.

Kontaktadresse:

Richard Hann, Department of Engineering Cybernetics (ITK), Norwegian University of Science and Technology (NTNU), Trondheim
Tel.: + 47 48020891, E-Mail: richard.hann@ntnu.no

Arbeit ausgegeben am: 01.11.2023
Arbeit abgegeben am:
Note festgelegt am:

Betreuer:
Richard Hann (ITK / NTNU)
Jan Pfaff (IFB / Universität Stuttgart)

03.07.2023
....
Datum

....
(Prof. Dr.-Ing. A. Strohmayer)

Kurzfassung

Unbemannte Luftfahrzeuge (UAVs) haben sich dank ihrer flexiblen Einsatzmöglichkeiten, Kosteneffizienz und Sicherheitsvorteilen in den verschiedensten Branchen etabliert. Trotz ihrer zahlreichen Vorteile stehen UAVs vor wettertechnischen Herausforderungen, u.a. atmosphärische Vereisung während des Fluges. Daher werden Experimente zur Eisbildung in speziellen Vereisungswindkanälen durchgeführt, in denen solche atmosphärischen Bedingungen simuliert werden. Diese Tests ermöglichen es, das potenzielle Risiko einer Vereisung während des Fluges zu untersuchen und besser zu verstehen. In dieser Studie wurde eine Methodik zur Digitalisierung der daraus resultierenden Eisformen entwickelt, um das Ausmaß und die Verteilung der Eisansammlung auf den Oberflächen von UAV-Komponenten zu quantifizieren. Als Grundlage dazu diente das photogrammetrische Verfahren „Structure-from-Motion". Hierbei werden mittels einer speziellen Software digitale 3D-Modelle der Eis-Geometrien basierend auf sich überlappende 2D-Bilder erstellt. Die vorgestellte Methode umfasst dabei alle Schritte, von der Erzeugung der Eisansätze im Vereisungswindkanal, über deren Bildaufnahme und 3D-Rekonstruktion bis hin zur Auswertung zur Bestimmung von Eis-Dicke, -Volumen und -Dichte. Die digitalisierten Eis-Geometrien wurden mithilfe von sog. „Global Control Points" skaliert und referenziert, welche über bekannte Koordinaten verfügen und so eine Transformation von einem relativen, digitalen Koordinatensystem in ein reales, physisches Koordinatensystem ermöglichen. Darüber hinaus wurde die Genauigkeit der Methodik untersucht und Maßnahmen ergriffen, um das Prinzip der Digitalisierung von Eis-Geometrien mittels Photogrammetrie besser zu verstehen und weiter zu verfeinern.

Abstract

Uncrewed aerial vehicles (UAVs) have been established in various industries thanks to their flexible application options, cost efficiency, and safety advantages. Despite their numerous benefits, UAVs face challenges in the occurrence of atmospheric icing during flight. Experiments on ice accretion are performed in icing wind tunnels, in which such atmospheric conditions are simulated. These tests allow to investigate and understand the potential risk of in-flight icing. In this study, a method was developed to digitize the resulting ice shapes to quantify the extent and distribution of ice accretion on the surfaces of UAV components. For this purpose, the photogrammetric technique "Structure-from-Motion" is applied. Using special software, digital 3D models of the ice geometries are created based on overlapping 2D images. The method presented includes all steps, from creating the ice shapes in the icing wind tunnel to their image acquisition and 3D reconstruction to the post-processing to determine, e.g., the ice thickness, volume, and density. The digitized ice geometries were scaled and referenced using so-called "global control points," which have known coordinates and thus enable a transformation from a relative, digital coordinate system into a real-world, physical coordinate system. In addition, the accuracy of the methodology was investigated, and measures were taken to better understand and further refine the principle of digitizing ice shapes using photogrammetry.

Contents

List of Abbreviations

Abbreviation	Description
2D	two-dimensional
3D	three-dimensional
API	application programming interface
BVLOS	beyond visual line of sight
CAD	computer-aided design
CCD	charged coupled device
CFD	computational fluid dynamics
CMOS	complementary metal-oxide-semiconductor
CSV	comma-separated values
FFF	fused filament fabrication
GCPs	global control points
GUI	graphical user interface
ICAO	International Civil Aviation Organization
IFB	Institute of Aircraft Design
IPS	ice protection system
IR	infrared
IWT	icing wind tunnel
JPEG	Joint Photographic Experts Group
LWC	liquid water content
MCCS	maximum combined cross section
MVD	mean volume diameter
NASA	National Aeronautics and Space Administration
NTNU	Norwegian University of Science and Technology

Abbreviation	Description
PDF	probability density function
RAW	raw image format
RPM	revolutions per minute
SfM	Structure-from-Motion
SIFT	scale invariant feature transform
SLD	supercooled large droplets
SLS	selective laser sintering
STL	stereolithography
UAV	uncrewed aerial vehicle
USGS	United States Geological Survey
VLOS	visual line of sight
VTT	Technical Research Centre of Finland

List of Figures

List of Tables

1 Introduction

Uncrewed aerial vehicles (UAVs) have emerged as revolutionary tools across various industries, from military and surveillance to agriculture, environmental monitoring, and disaster relief [1]. Unlike manned aircraft, UAVs are piloted remotely or autonomously, offering flexibility, cost-effectiveness, and safety advantages in numerous applications and mission scenarios [2]. However, despite their numerous advantages, UAVs face challenges when operating in adverse weather conditions, particularly atmospheric in-flight icing [3]. In-flight icing occurs when supercooled water droplets freeze upon contact with the UAVs' surfaces, accumulating ice on the aircraft [4]. This effect alters the shape of aerodynamic surfaces, leading to reduced aerodynamic performance, increased weight, and potential loss of control [5]. The consequences of icing can compromise flight safety and mission effectiveness, posing significant risks to both the UAV and surrounding airspace.

To address these icing concerns, the UAV Icing Lab at the Norwegian University of Science and Technology (NTNU) studies UAV icing using a combination of numerical simulations, icing wind tunnel tests, and real flight tests. This multi-method approach aims to understand the physical basis of icing and its effects on various UAV components and develop effective anti-icing and de-icing solutions. One key aspect of this research is the investigation and evaluation of icing experiments. Digitizing ice shapes allows for quantifying the extent and distribution of ice accretion on the surfaces of UAV components. By converting physical ice shapes into digital formats, precise measurements of ice thickness, shape, and location can be obtained. This analysis helps to understand the aerodynamic effects of ice accretion, improve icing simulation models, and compare it with other studies.

Photogrammetry offers a promising and cost-effective approach to this task. It involves capturing multiple images of the ice formation from different angles and using specialized software to reconstruct a three-dimensional (3D) model of the ice shape [6]. This approach eliminates the need for expensive 3D measuring equipment, making it an economically attractive option for digitizing ice shapes.

Therefore, this work aimed to develop and optimize a process for digitizing and evaluating ice shapes from icing wind tunnel (IWT) tests through the application of photogrammetry. Furthermore, the research investigated the accuracy and reproducibility of the 3D reconstruction and explore associated limitations.

2 Theoretical Backround

2.1 Uncrewed Aerial Vehicles

The International Civil Aviation Organization (ICAO) states that an "UAV is a pilotless aircraft, [...], which is flown without a pilot-in-command on-board and is either remotely and fully controlled from another place (ground, another aircraft, space) or programmed and fully autonomous" [2]. UAVs were initially developed in the 1900s for military applications that were too "dull, dirty, or dangerous" [7] to be performed by humans. Because of these advantageous features, the technology has evolved significantly. Today, UAVs are an integral part of many defense forces worldwide [8]. As electronics and flight control software have advanced and thus become more affordable, UAVs have become popular in many civilian applications [1]. Frequent users of UAVs are in the construction and agriculture sectors, where UAV applications are used for surveying, stockpile volume measurements, and crop monitoring. Today's common UAV applications include photography, film, inspection, mapping, remote operations, research, and search and rescue [1]. Thus, UAVs come in various types and sizes, from micro UAVs to large, high-flying UAVs comparable in size to passenger transport aircraft [7].

One key distinction of UAV operations is between missions flown within visual line of sight (VLOS) and beyond visual line of sight (BVLOS). Until recently, most UAVs have been operated under VLOS operation. Here, the pilot can see the UAV and control it manually if the autopilot fails [9]. To extend the range and scope of potential missions, the development of future UAVs is increasingly focused on operation under BVLOS conditions. This requires a higher degree of automation of the UAV since it cannot be directly seen and controlled by the operator. Therefore, it must be able to perform a mission independently and adapt it to the corresponding circumstances [4]. An important aspect to consider for any UAV that is supposed to operate BVLOS is how to deal with challenging weather conditions, such as atmospheric icing [4].

2.2 Atmospheric In-Flight Icing

Icing on aircraft is a severe hazard that has led to numerous crashes on aircraft [10]. It can be divided into two primary categories: ground icing, which refers to the accumulation of ice and snow on the ground before take-off, and atmospheric in-flight icing [4]. Assuming that UAVs can be well protected from icing on the ground, this case will not be discussed further in this thesis.

In-flight icing can pose a major threat to the reliable operation of UAVs [4]. Atmospheric in-flight icing is a term for a meteorological condition where supercooled liquid water (water temperature below the freezing point) exists in the atmosphere, mostly occurring in clouds (in-cloud icing) or less often in precipitation [9]. These conditions can occur year-round in polar regions but also in temperate climates, most frequently in winter [11]. A climate analysis of Norwegian airspace and surrounding areas has shown that large geographical areas are exposed to potential icing of more than 50 % from October to February [3]. The color chart in Figure 2.1 signifies the time share when potential icing conditions are present for each of the twelve months. Red indicates a high risk of icing conditions, whereas white suggests a low risk.

When such supercooled droplets collide with an aircraft, they either freeze instantly or create a water film moving along the surface, which can also freeze, forming various ice shapes [4]. The process of water attaching to the surface is called impingement [4]. Environmental factors determining ice accretion rate include air temperature, liquid water content (LWC) in clouds, and droplet size, often expressed in mean volume diameter (MVD) [12]. In addition, the aircraft's shape, size, and velocity influence the ice accretion [12]. The resulting ice shapes can be categorized into several ice types, which are briefly introduced in Figure 2.2 below:

- Rime Ice

- Glaze Ice

- Mixed Ice
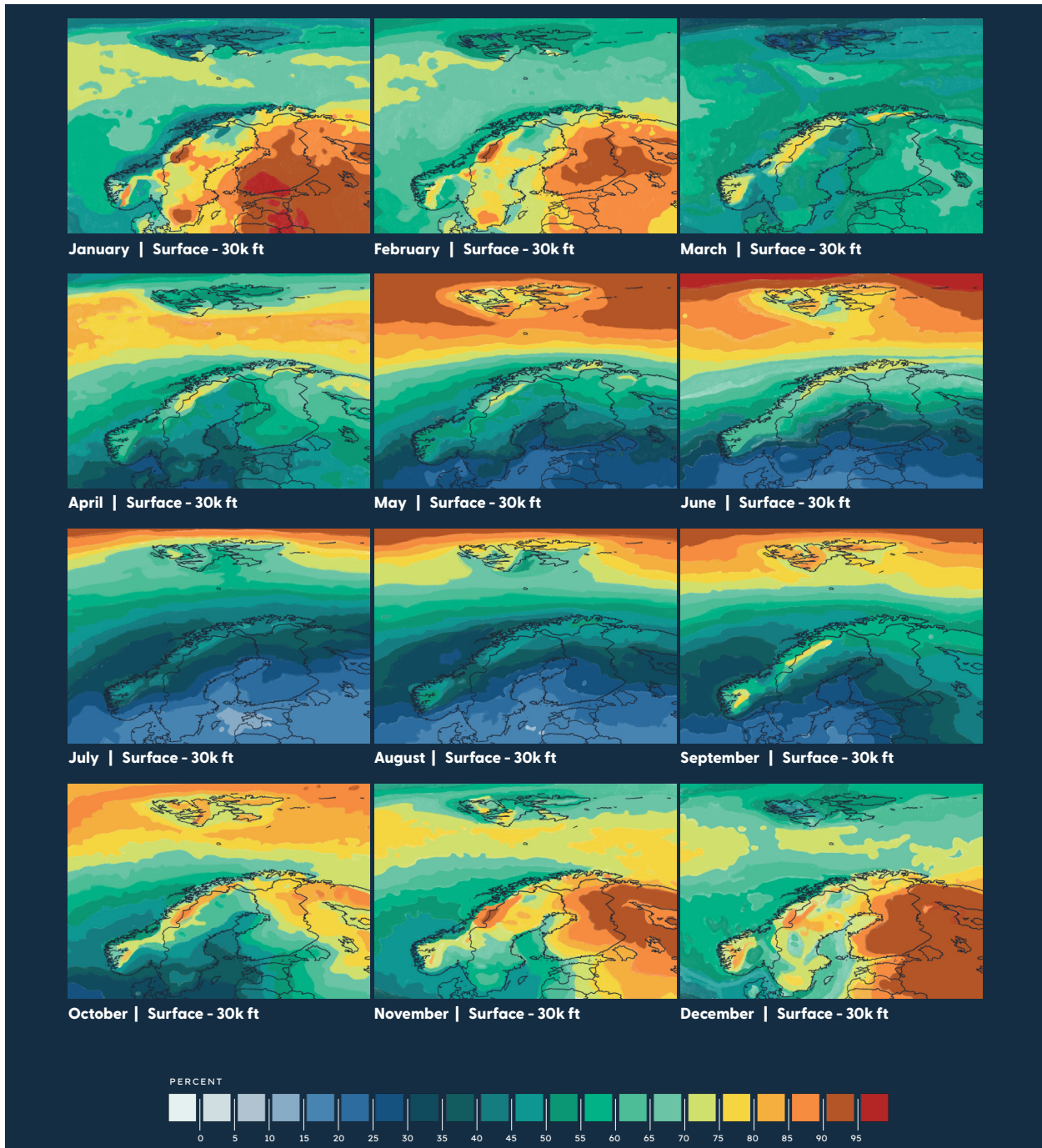
Figure 2.1: Potential icing frequencies of Norwegian airspace and surrounding areas [3].
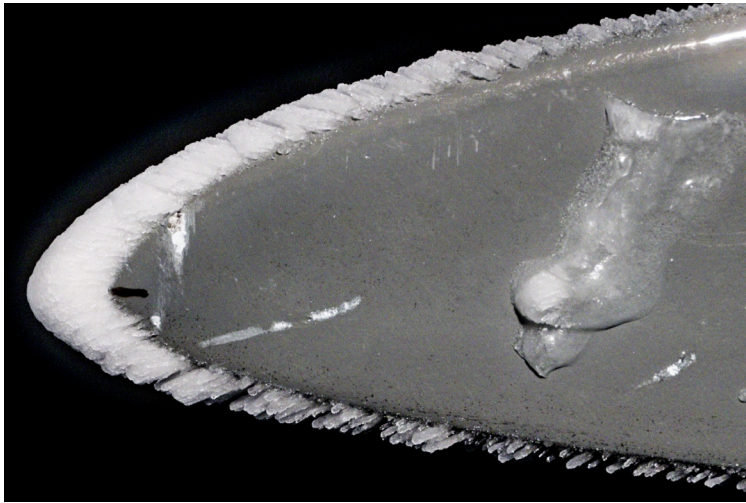
Rime ice forms at very low temperatures, causing the droplets to freeze instantly when they collide with a surface. This process creates an ice shape with a rough surface and a streamlined geometry. Since the droplets freeze so fast, small air pockets are trapped between the freezing droplets, which gives rime ice its characteristic white appearance. Rime ice typically results in moderate aerodynamic penalties [4].
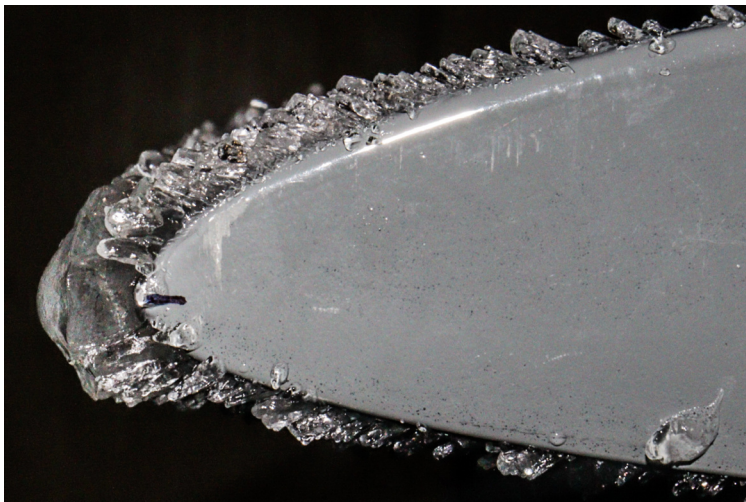
Glaze ice, also called clear ice, forms at temperatures near the freezing point. In this temperature regime, the incoming droplets remain in their liquid phase longer and do not freeze instantly. The resulting liquid water film steadily freezes on the surface, forming transparent ice shapes. Glaze ice shapes can create complex geometries, leading to severe aerodynamic penalties [4].

Mixed ice typically occurs in the temperature range between rime and glaze and combines both ice forms. Some droplets that hit the surface freeze immediately, and some remain liquid. The latent heat released during the icing or aerodynamic heating can also support this process. The geometries that form during mixed ice vary considerably in shape and can lead to severe aerodynamic penalties [4].

Figure 2.2: From top to bottom: Rime ice, glaze ice, and mixed ice [4].

Other Icing Conditions

Besides these classic in-cloud-icing phenomena, there are several other icing conditions, predominated by freezing precipitation. Freezing precipitation can have a much more severe impact on aircraft due to the large droplets. Compared to cloud droplets with an MVD of about 40 - 50 μm, the size of the droplets can reach a diameter of several millimeters, which is why they are also known as so-called supercooled large droplets (SLD) [4]. SLD icing conditions can lead to rapid ice accretion rates, resulting in a substantial performance penalty in a very short time [13]. Snow and ice crystals usually pose a lower threat to larger aircraft because aircraft with fixed-wing configurations generally fly at such high speeds that snow and ice crystals are unable to stick to their surface. However, wet snow can settle on the structures of slower-moving aircraft such as quadrocopters, leading to a significant increase in weight and mechanical failure [4]. A third phenomenon is cold soaking, which can occur when an aircraft descends from high altitudes and encounters precipitation. The fuel stored in the wings, which has cooled down during flight, cools the wing to temperatures below freezing so that icing can occur even at air temperatures above freezing point [9].

2.3 In-Flight Icing Effects on Aircraft

Icing can affect the safe operation of UAVs on several levels:

Sensor Blockage
First, a critical system concerning icing is the pitot tube, which indicates the aircraft's airspeed. Due to its small size, the pitot tube can quickly become clogged with ice, providing erroneous sensor measurements to the control system. This, in return, can lead to incorrect flight behavior and even to a potential loss of the aircraft. Other sensors like camera lenses, antennas, and radomes can also be affected by icing [10].

Mass Increase
Second, ice mass accumulating on the wings adds significant weight to the aircraft, resulting in higher mechanical loads and requiring more drive power simultaneously [14]. The additional weight can quickly become critical, especially for small aircraft, since they mostly have more stringent weight restrictions. Further, the extra weight can negatively affect the center of gravity, and therefore stability and aircraft maneuverability [3].

Propulsion Degradation
Third, icing affects the aircraft propulsion system. For combustion engines, it may block the engine inlets. Propellers are particularly affected by icing because they can accumulate large amounts of ice quickly, which can lead to significant efficiency losses. Figure 2.3 shows that propellers can lose up to 70 % of their trust in icing conditions within 2 minutes [3]. Furthermore, the increased weight leads to higher mechanical stress on the propeller. As a result of the high centrifugal forces, single ice fragments can be thrown off the propeller blades. This causes imbalances in the rotor dynamics and strong vibrations that can

damage the engine [3].
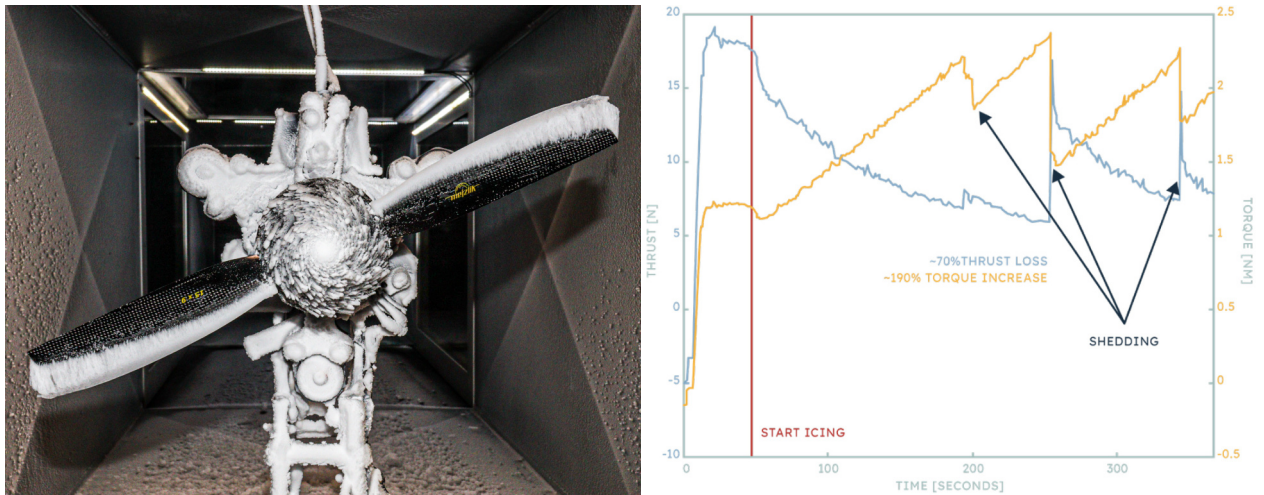
Figure 2.3: Propeller performance degradation in moderate icing conditions in an icing wind
tunnel [3].

Degradation of Aerodynamic Performance
Lastly, ice accretion on aerodynamic surfaces affects the aerodynamic performance by generating less lift and more drag. This can also lead to stalling at smaller angles of attack than regular operational conditions as shown in Figure 2.4(b) [3, 4]. In general, ice on airfoils can be separated into four different ice morphologies, shown in Figure 2.4(a) and presented below.

(a)   (b)
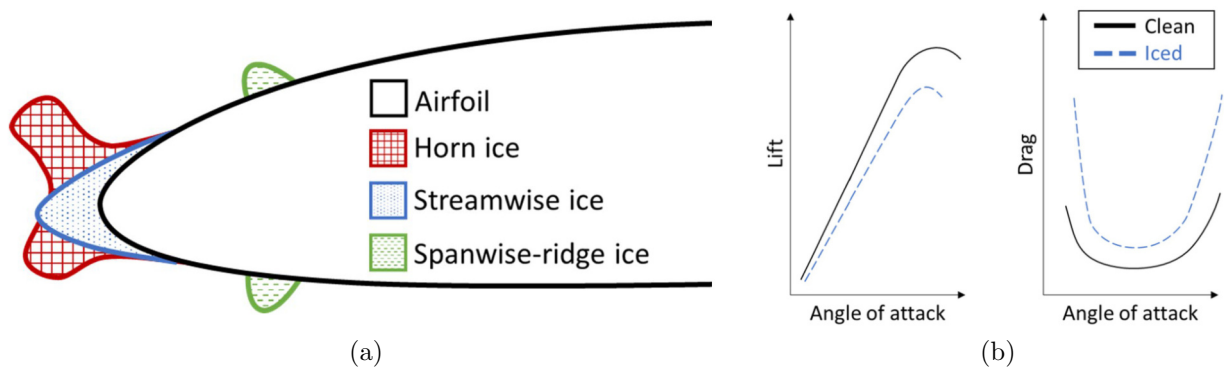
Figure 2.4: (a) Typical ice morphologies on an airfoil and (b) qualitative aerodynamic performance degradation due to icing [4].

Ice Roughness
Ice roughness occurs during the initial stages of the ice accretion process, forming a thin and rough ice layer that increases skin friction and can cause early laminar-turbulent transitioning of the boundary layer [4, 5].

Horn Ice
Horn ice mainly develops under glaze ice conditions. It is characterized by protruding horn features counter to the direction of flow that leads to flow separation at the top of the horns. This leads to an early laminar-turbulent transition, increased pressure drag, and reduced lift [5].

Streamwise Ice
Streamwise ice typically forms during rime ice conditions and results in streamlined ice shapes. This ice type's effect is much smaller than horn ice or spanwise-ridge ice since leading-edge separations found to be small [5].

Spanwise-Ridge Ice
Spanwise-ridge ice is a special icing condition that occurs in combination with an ice protection system (IPS) that only protects the leading edge of the wing. Water flows back on the surface from the heated section to freeze downstream on the cooler unheated surface. This happens especially in SLD conditions or if the IPS does not completely evaporate the impinging droplets. Ridges are generally located farther downstream than the other ice types, allowing the boundary layer to develop along the airfoil. Compared to horn and streamwise ice shapes, which rather act like a backward-facing step flow, the spanwise-ridge ice has characteristics of a flow obstacle. Therefore, it can have the most significant effects on the aerodynamic performance [5]. Furthermore, SLD and runback icing may extend to control surfaces, decreasing their effectiveness or blocking them [4].

Icing Challenges for UAVs

Due to their technical characteristics, UAVs face a number of unique challenges compared to manned aviation:

Size
UAVs are typically smaller than crewed aircraft. Deflection forces that influence a droplet's trajectory depend on the size and shape of the airfoil [4]. Smaller airfoils have a lower effect on the flow field and a lower deflecting impact on the droplets. This results in a greater impingement rate of droplets and, thus, faster ice accretion [9]. Additionally, the ice shapes appear more extensive in relation to the smaller dimensions, and the aerodynamic performance degradation is more critical than with larger aircraft [12].

Flight Velocity

Due to their smaller size, different mission profiles, and propulsion concepts, UAVs typically operate at lower flight velocities than crewed aircraft. This results in negligible aerodynamic heating and reduced suction pressure, making icing occur at a broader range of temperatures. Additionally, high airspeeds and friction cause higher shear stresses and pressure differential. This promotes ice accumulation to shed, enhancing the efficiency of IPSs. Due to lower airspeeds, UAVs experience less efficient ice shedding by the IPS than crewed aircraft [9].

Reynolds Number

The Reynolds number is a dimensionless number that describes the ratio between inertial and viscous forces (momentum). It is used to characterize the transition from laminar to turbulent flow. UAVs typically operate lower at Reynolds number regimes due to their smaller sizes (chord lengths) and lower operational velocities. Therefore, laminar flow is more prevalent. Laminar flow is more sensitive to surface contamination. Thus, the ice and surface roughness lead to higher penalties than turbulent flow [9].

Energy

Small UAVs are usually powered by batteries or combustion engines. While larger aircraft can use bleed air from turbine engines for their IPS, small aircraft often rely on electrothermal IPS. Electrothermal IPS can require high currents, necessitating modifications to the aircraft's power system and severely affecting the UAV's flight endurance. Aircraft without IPS require more thrust to compensate for aerodynamic degradation, while aircraft equipped with IPS become heavier and require additional power to combat icing [9].

Control Systems

Future UAVs are being developed with the aim of fully automated systems. Thus, control systems require sensors to detect ice because an onboard pilot is not available for visual observations. Furthermore, they must be capable of adapting to in-flight icing threats by increasing speed, reducing altitude, or changing paths for safe operation under all weather conditions [9].

To ensure the safe operation of UAVs, it is essential to deal with the issue of atmospheric icing and take appropriate measures to detect, avoid, and prevent it. This task requires a multi-method approach, including simulations and experimental tests in IWTs. To evaluate and compare these tests, the extent and distribution of the ice accretion on aerodynamic surfaces must be quantified. By converting physical ice shapes into digital formats, precise measurements of ice thickness, shape, and location can be obtained. Photogrammetry provides a promising approach for this matter.

2.4 Structure-from-Motion Photogrammetry

Photogrammetry describes the science and methodology of capturing and analyzing images to reconstruct objects' texture, shape, and position [15]. Structure-from-Motion (SfM) is a photogrammetric technique to reconstruct 3D structures from a collection of two-dimensional (2D) images. When an observer moves, the surrounding objects move differently depending on their distance from the observer, providing additional information about the depth/distance of each object. This phenomenon, called motion parallax, is a principle for humans and many animals to gain 3D details about their environment. Pigeons for example, whose eyes do not have overlapping fields of view and thus cannot use stereopsis, gain visual depth by dynamically moving their head [16].

Like animals use different viewpoints to perceive depth, computer algorithms can establish a line of sight to key points, called features, on an object for additional views [17]. These features are distinctive points in the images, such as corners, edges, or unique patterns [17]. SfM solves the key issue of determining the 3D position of corresponding points found in the 2D images. A widely used solution to this is object recognition using scale invariant feature transform (SIFT) [6]. This algorithm, invented by David Lowe in 1999, proved very robust to significant image variations, making it suitable for this application. SIFT uses a multi-step process to analyze the images at multiple scales and rotations. Key points are automatically detected across all scales and locations within each image (Figure 3.5). Subsequently, feature descriptors are generated by transforming local image gradients into a representation largely immune to illumination and orientation variations [18].

The next step is matching these distinctive descriptors between the images. This enables estimation of the camera pose of each image and reconstruction of the 3D scene by triangulating the matched key points from multiple images [6]. At the intersection of various lines of sight, an approximation of the 3D coordinates for a specific point is determined (Figure 2.5). The result is a low-density or "sparse" point cloud fixed into a relative coordinate system. Bundle adjustment is usually done to further refine the initial SfM model iteratively [19]. The term "bundle adjustment" comes from the idea of adjusting the entire bundle of rays that project from the 3D scene points to the corresponding image points. The optimization process aims to minimize the difference between the observed image points and the projected 3D points based on the refined camera poses and structure [20].

Based on the calculated camera positions a "dense" point cloud can be estimated by calculating depth values for every pixel in the images and, hence, depth maps for each image. A digital 3D model of the object is finally gained by meshing the point cloud.
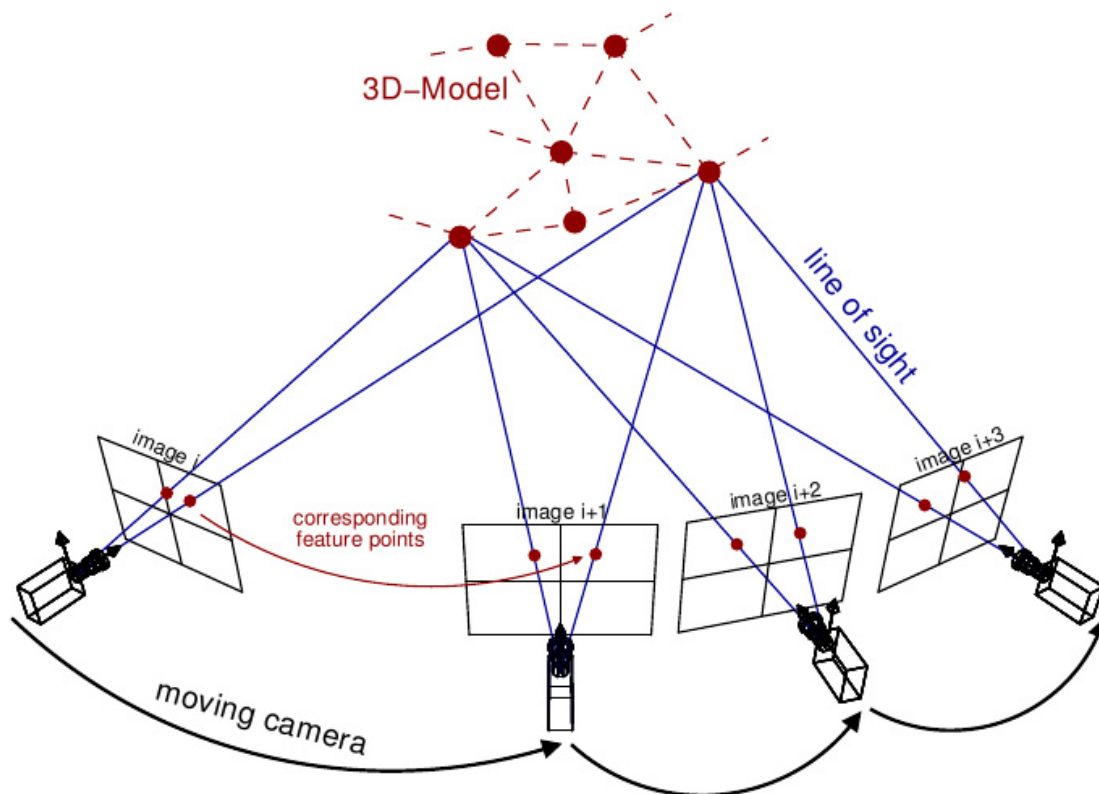
Figure 2.5: Perceiving depth by tracing lines of sight from different viewing angles [21].

Data Acquisition

The essential requirement for the 3D reconstruction of an object via SfM is a set of 2D images taken from different angles and preferably featuring a high degree of overlap [6]. As increasing the number of lines of sight results in higher system redundancy and, thus, greater confidence in the 3D coordinates of the associated point, it is generally recommended to use as many images as possible. To obtain information about the entire object, it is also necessary to photograph it from all sides (Figure 2.6). However, more images come at the expense of storage and processing and can lead to uneconomically long computing times [6]. A diverse range of imaging sensors can be used for SfM, from video stills to low-grade compact digital cameras. The critical factor for successful results is well-exposed photographs featuring the points of interest. The number of key points in an image is mainly influenced by image texture and resolution. Consequently, intricate photos at higher resolutions, preferably the original ones, yield more results. The quality of the output point cloud data is primarily determined by the density, sharpness, and resolution of the photoset, along with the variety of natural scene textures [6].
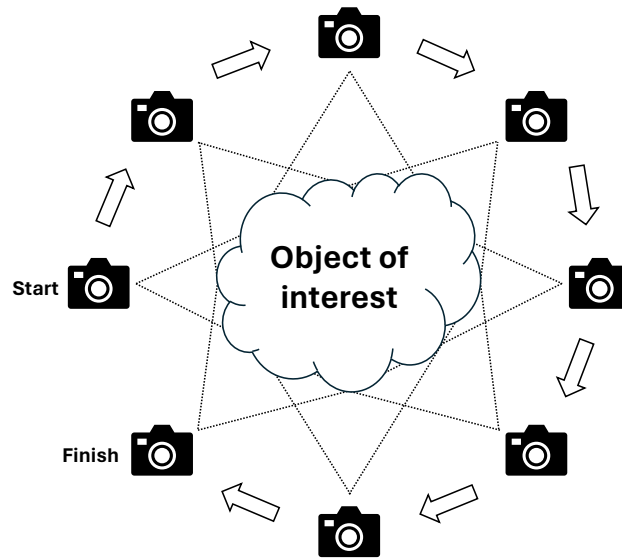
Figure 2.6: Capturing an object from many angles with sufficient overlap between images is necessary for usable output. Adapted from [6].

Model Referencing

Since neither the camera positions nor the 2D images necessitate real-world coordinates, the 3D point cloud produced via SfM photogrammetry is established within a relative "image-space" coordinate system and, therefore, lacks information on scaling and orientation [6]. The transformation of the point cloud from this relative image-space coordinate system to a real-world "object-space" coordinate system is usually achieved through so-called global control points (GCPs). These points have known object-space coordinates and are used to scale and reference the models. [6].

GCPs can be either natural, such as corners or edges, or artificial, meaning they are specifically designed and placed for the survey. The distinctive appearance of artificial markers, which are highly contrasted to their surroundings, reduces the likelihood of misidentification [6]. Modern GCPs designs are often based on binary coding, enabling unique identification of individual markers. Some examples are shown in Figure 2.7. The standardized uniqueness of binary fiducial markers also facilitates the automation of the marker detection process [22]. However, these advantages come with the cost of additional effort and expense, as these markers need to be manually set up before image acquisition.

The model can be referenced by specifying at least three GCPs [23]. A single reference point defines the scene origin, two points define origin and scale, and a minimum of three points is required to specify complete scene orientation. Increasing the number of GCPs improves the quality of the photogrammetric output and redundancy [24].

(a) Schneider, 1991   (b) Ahn, 2001   (c) arUco, 2014
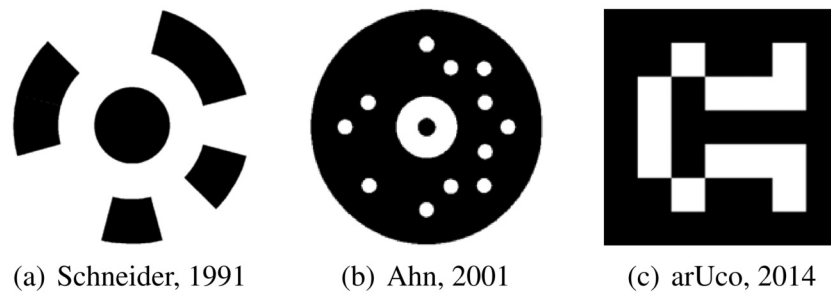
Figure 2.7: Examples of coded targets commonly employed in photogrammetry applications [22].

2.5 Digital Cameras and Settings

Digital cameras capture images electronically, transforming scenes into digital data that can be stored, processed, and shared. Unlike film cameras that use chemical processes to record images on film, digital cameras employ sensors to convert light into electrical signals, creating a digital representation of the captured scene [25]. The camera's internal components then process these signals to generate digital photographs. Imaging sensors work due to the photoelectric effect which causes electrons to emit from materials when hit by electromagnetic radiation and, thus, electrical charges [26].

Most digital cameras use either a charged coupled device (CCD) or a complementary metal-oxide-semiconductor (CMOS) as image sensor. In CCD sensors each pixel consists of a metal–oxide–semiconductor capacitor. The technology involves the movement of electrical charge through a series of capacitors and a single output amplifier. In contrast each pixel in a CMOS sensor has its own individual amplifier and is capable of converting light into an electrical charge independently. In general, CCD sensors produce higher-quality, low-noise images with increased light sensitivity, whereas CMOS sensors are cheaper, offer faster processing, and consume less power [26].

Digital cameras come with various settings and features to capture the scenery. The most important are:

- **Resolution:** Determines the number of pixels in an image. Higher resolution results in sharper and more detailed images [17].

- **ISO Sensitivity:** Controls the sensors's sensitivity to light. Higher ISO values are helpful in low-light conditions but may introduce more noise (Figure 2.9 - 2.12) [17].

- **Aperture:** Regulates the size of the lens opening. Sets depth of field and the amount of light entering the camera (Figure 2.9 - 2.12). Smaller Apertures (or higher "f-stop" in the camera settings) enhance depth of field but reduce the amount of light that hits the sensor [17]. Too small aperture sizes can also cause diffraction effects [27].

- **Shutter speed:** Governs how long the camera's shutter remains open and, thus, the duration that light passes through (Figure 2.9 - 2.12). Faster shutter speeds freeze motion, while slower speeds capture motion blur [17].

- **White Balance:** Adjusts the color temperature of the image to compensate for different lighting conditions [17].

- **Focus Mode:** Determines how the camera focuses, whether automatically, manually, or in combination [17].

Finding the correct settings always depends on the scene to be filmed and requires some experience, as these parameters partly influence each other. Achieving optimal exposure and capturing well-balanced images involves a dynamic relationship among the ISO, shutter speed, and aperture values. Each click or stop-change in either of them halves or doubles the amount of light that reaches the sensor. Thus, if one action cuts the light by half, then it must doubled in another to retain the same level of brightness in images (Figure 2.8) [17].
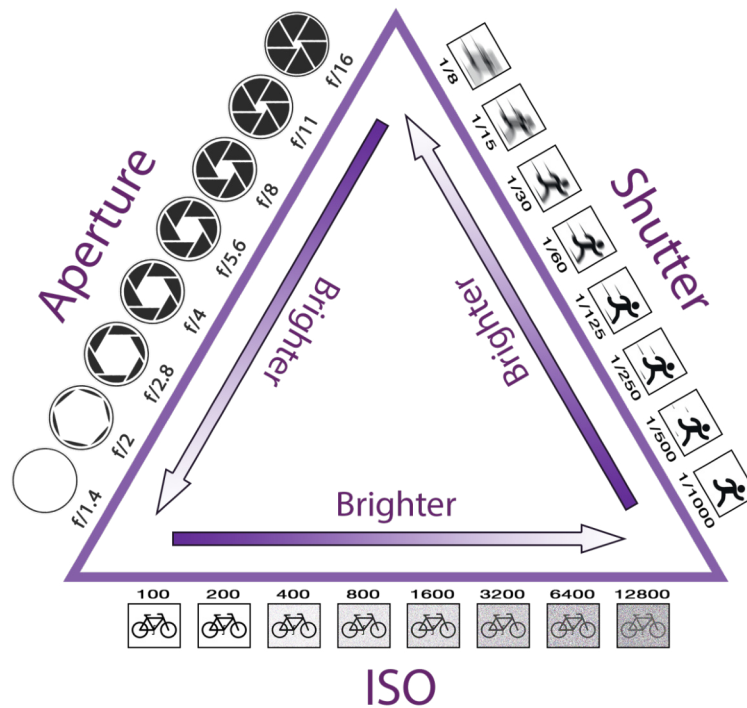
Figure 2.8: The Rule of Equivalent Exposures: By cutting the light by half in one way, it must be doubled in another to retain the same level of brightness [17].

Figure 2.9: The impact of ISO sensitivity on the image quality. Pictures made with ISO value set to (a) 100 and (b) 65535 with equivalent exposures and same aperture sizes.

Figure 2.10: The impact of changing the aperture on depth of field and focus. Pictures made with aperture sizes set to (a) $f/16$ and (b) $f/1.8$ with equivalent exposures and same ISO value.
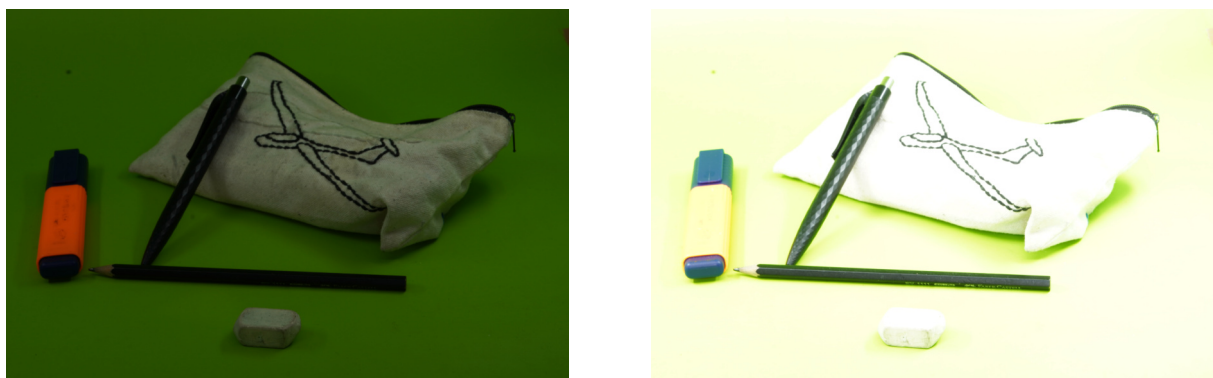
Figure 2.11: The impact of the shutter speed on exposure. Pictures made with shutter speeds set to (a) 1/15 sec and (b) 2 sec with same aperture size and ISO value.

2.6 State of the Art

Various methods have been developed for measuring and digitizing ice shapes. The most common are presented below:

Hand Tracing
Simple hand tracing has been the most widely used ice measurement technique since it is simple and inexpensive. For this purpose, a slice of ice is cut out by a heated plate and traced on the paper, which is scanned to digitize the traced line. This method is not only highly dependent on the experience and skills of the experimenter and the tracing tool used. It is also only possible to examine 2D cross sections for evaluation [28].

2D Photography
An alternative approach to hand trace the cut ice shapes involves using 2D photography, where the cross-sectional view of ice accretion is captured along with a reference object for scale [29]. Again, only two-dimensional measurements are possible. Furthermore, potential sources of error arise if photographs are taken from an inclined perspective, if the desired plane is out of focus, or if ice is captured outside the desired plane [28].

Mold-and-Cast
The mold-and-cast principle is a reasonably established and accurate method for documenting ice shapes. A silicone mold of the ice accretion is produced from which a cast can be made using a two-component polyurethane mixture [30]. This method allows the precise creation of artificial ice shapes, which can then be examined under non-climatic conditions and digitized, e.g. by industrial 3D scanning techniques [31]. However, shrinkage errors can occur during curing, and the molds are generally delicate to handle [32].

Structured Light Scanning
Structured light 3D scanning works by projecting laser light stripes onto the surface of the ice shape and then capturing images of it with one or more cameras. The scanner can reconstruct the ice shape by analyzing how the projected pattern deforms. While this method works well for rime ice, the number of needed detectors increases with more complex ice structures due to shading [33].

Optical Laser Scanning
Laser scanning is an optical range measurement method based on the triangulation principle to reconstruct the 3D geometry [28]. Nowadays, it is one of the most common methods for digitizing ice due to its high accuracy and ease of use [28, 31]. Therefore, it is often used to validate other methods [32, 34]. Gong and Bansmer also developed a process for the dynamic measurement of ice growth during the icing experiment based on optical laser sheet scanning [28]. However, the accuracy of laser scanning is highly dependent on the optical properties of the ice. Due to its reflectivity, the ice must be coated with opaque colors or powders, which can affect the result [35].

Mid-infrared (IR)-Laser Scanning
As a further improvement, mid-IR 3D laser scanning was investigated. It works on the same principle as optical laser scanning but in a longer wavelength range (8-14 µm). The reflectivity of ice is significantly lower in this wavelength range compared to the visible spectrum. Therefore, mid-IR eliminates the requirement of spraying opaque dyestuff on the ice surface [35].

Tomography
Although optical scanning techniques allow for observing macroscopic ice geometry features, measurements of small details, such as ice feathers, are challenging as these are partially concealed. Investigations were therefore carried out to digitize these details using tomography [32]. It works by exposing a sample to an X-ray beam, capturing the resulting radiography image, and converting it into visible light using a scintillator. The image is then magnified optically and captured by a CCD detector. The magnification allows minor details to be visible. Multiple reconstructions create a 3D representation [32].

Stereo-Photogrammetry
McKnight was the first to use photogrammetry for quantitative icing research by taking stereo-photographs during flight. Although this achieved satisfactory spatial accuracy, the method only provided 2D ice-shape profiles. Moreover, the claimed accuracy only applied to rime ice, as glaze ice was not identifiable due to its transparency. For usable photographs, the aircraft had to leave the cloud, as the cloud droplets' backscattering of the light from the flash produced unusable imagery [36].

Structure-from-Motion Photogrammetry
The accuracy of the previously mentioned techniques is directly related to the level of resources invested in hardware, potentially leading to expensive experimental setups. SfM photogrammetry provides a relatively cost-effective approach for digitizing ice shapes since standard cameras can be used to get the data, and the knowledge focus is on the SfM algorithms [34]. Previous studies have applied SfM photogrammetry for digitizing ice accretion, noting that the approach "has shown to be very sensitive to the optical properties of ice" [4]. Especially glaze ice caused poor results due to its reflectivity. Coloring the specimens, however, significantly improved the results as long as the color was sufficiently dried in a freezer [4].

Ice Measurement at the UAV Icing Lab

The method of SfM photogrammetry has also been used by the UAV Icing Lab. However, the process has only been carried out experimentally and individually, lacking a standardized process. This leads to significant differences in the quality of the results. Major difficulties have previously been encountered in scaling and referencing the reconstructed 3D models carried out manually in computer-aided design (CAD) programs. This method is time-consuming and hardly allows an accurate comparison with plain geometry since the referencing must be performed in all six degrees of freedom.

Further research on digitizing ice shapes using photogrammetry was done at Braunschweig Icing Wind Tunnel at the Technical University of Braunschweig, where GCPs were used to scale and reference the model. The results were compared with the 3D scanning of the mold-and-cast measurement method. The study demonstrated photogrammetry as a promising method for capturing ice geometries as well as surface roughness [34].

Therefore, this work aimed to develop an optimized, standardized, reproducible, and simplified process to perform SfM photogrammetry to digitize ice shapes. Furthermore, it was investigated how accurately the ice shapes can be reconstructed using this method. The development of the technique is presented in the following chapter.

3 Method

Icing affects the safe operation of UAVs on several levels, as already stated in chapter 2.3. Concerning the degradation of the aerodynamic performance, two components are particularly affected: Propellers and lifting surfaces. The icing of propellers reduces thrust, drastically increases the required power, and can lead to structural overloading. On the other hand, icing on lifting surfaces and airfoils increases drag, decreases lift, and reduce stall margins. Accordingly, the photogrammetry method must also be able to digitize both components when they are tested in an IWT. This poses several challenges for the methodology, as these can differ significantly in terms of geometry, size, and icing morphology. Nevertheless, an attempt was made to develop a generally valid method for digitizing ice shapes on various components.
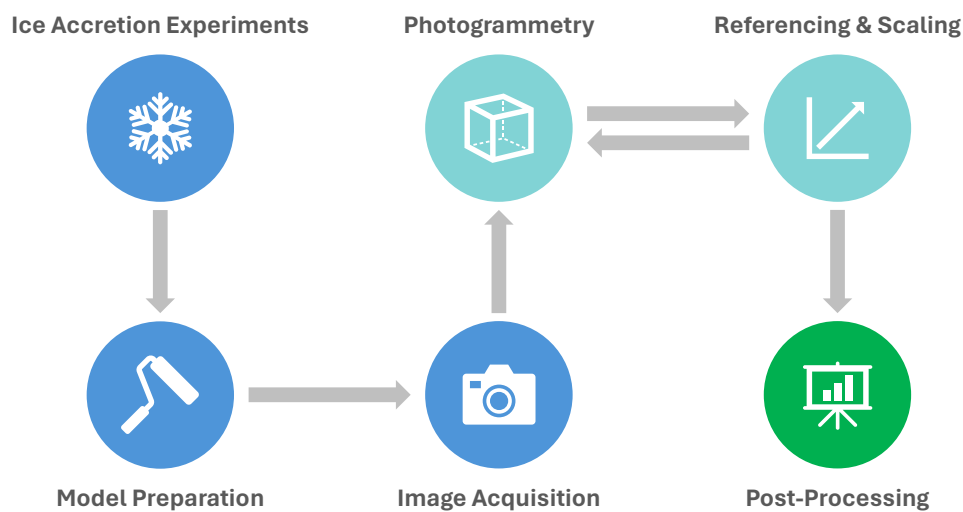
Figure 3.1: Procedure for the digitization of ice geometries using SfM Photogrammetry.

Figure 3.1 shows an overview of the procedure for digitizing ice geometries. Icing conditions on propeller blades or airfoils were simulated in an IWT. The test specimens covered with ice were then colored with opaque paint to avoid reflections and improve the quality of the images. Afterward, they could be photographed. All steps up to this point were carried out under controlled climatic conditions in the IWT. Based on the generated data, the photogrammetric 3D reconstruction of the ice geometries could be performed in the next step. Before exporting the digitized model, it needed to be scaled and referenced. This

was done using artificial GCPs with known coordinates attached to the test specimens and detected by the photogrammetry software. The finished model with a defined pose and size could then be analyzed and evaluated using various post-processing methods. Details on the specific steps are presented in the subsequent sections.

3.1 Ice Accretion Experiments

Experimental testing of icing conditions is crucial in designing aircraft capable of all-weather capabilities. IWTs offer the chance to simulate these conditions under laboratory conditions with defined parameters such as temperature, MVD, and LWC, thus comparing the results with those of numerical methods such as computational fluid dynamics (CFD) simulations. Typically, two main types of tests are conducted in IWTs: ice accretion experiments to identify worst-case icing conditions and functionality tests for sensors or IPSs [4].

IWTs share similarities with conventional wind tunnels but require additional elements. These include controlling temperature, maintaining subzero conditions for extended periods, and injecting water with controlled flow rates and specified droplet distributions. Various IWT designs exist, primarily developed for manned aircraft applications. However, challenges arise when applying these tests to UAVs, as the minimum airspeed achievable in IWTs often exceeds UAV flight speeds. Additionally, the high costs of renting facilities designed for certifying large passenger aircraft pose financial challenges. Therefore, the selection of potential IWTs for testing icing on UAVs is limited [4].

Some smaller IWTs are also available with lower airspeeds. An example is the IWT facility at the Technical Research Centre of Finland (VTT) in Helsinki. This facility operates in an open-loop configuration, offering continuous wind speeds of up to 20 m/s and short-term speeds reaching 50 m/s, which fits the low-speed requirement of UAVs (Figure 3.2) [37].
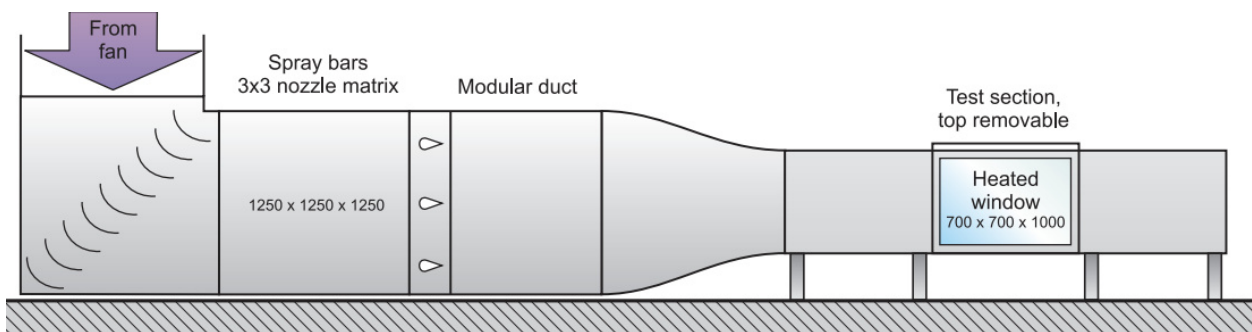
Figure 3.2: Schematic layout of the icing wind tunnel at the VTT [37].

Figure 3.3 shows the experimental setup for ice accretion experiments on airfoils and propeller blades. Test specimens are usually standardized and either self-made by 3D printing or purchased. The setup for the airfoil consisted of a 3D-printed part that could be removed and placed on a stand for the subsequent photo session. The setup for the propeller was speed-controlled by an electric motor. The propeller was also detachable and was attached to a rack for photography.

| (a) | (b) |
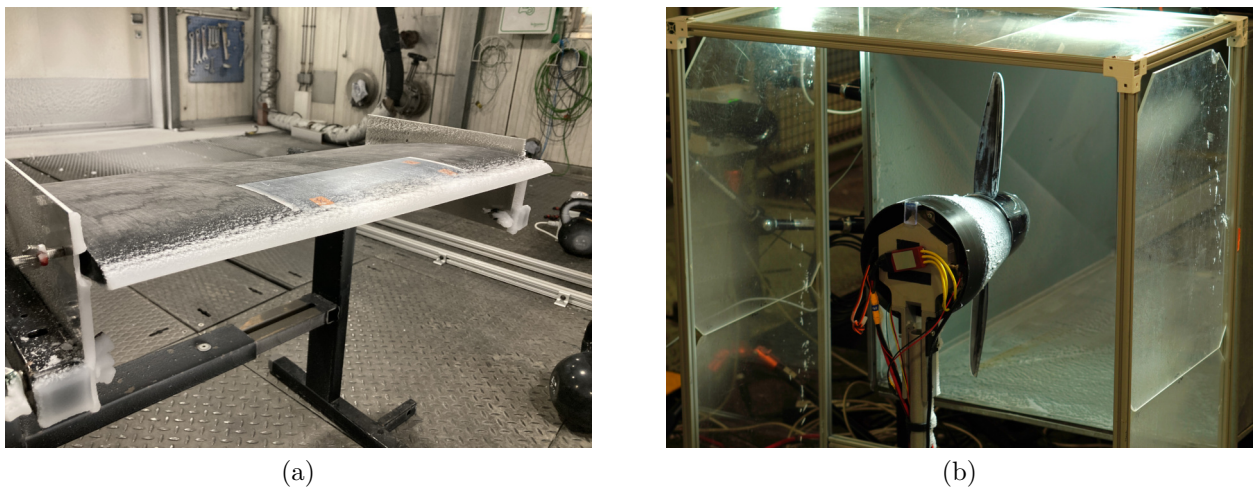
Figure 3.3: Setup for experimental icing wind tunnel tests on (a) an airfoil and (b) a propeller.

3.2 Model Preparation

As Hann [4] and others [28, 34] have already described in their work, the SfM approach proved very sensitive to reflective objects, leading to invalid results. Glaze ice, in particular, is highly reflective by nature. Therefore, ice shapes are usually colored with opaque spray paint or powder to digitize them [4, 28, 34]. To minimize the influence of the color application on the ice shapes, an airbrush was used. This method enabled a very even and thin painting. "Model Air White" by Vallejo [38] was the color used and diluted with water in a ratio of about 1:3.

Wet paint also proved to reflective and, therefore, difficult to evaluate. When testing at higher temperatures (around -2 °C to -4 °C), where the color particles do not freeze immediately to the ice, the colored specimens were placed in a freezer at -15 °C for 15 minutes. Afterward, they could be photographed. This step was not necessary for tests at cooler temperatures below -4 °C.

3.3 Image Acquisiton

The measurement setup and the choice of tools used were primarily based on existing tools in the UAV Icing Lab and the previous SfM photogrammetry tests. In the course of this work this setup was constantly expanded and improved.

Figure 3.4 shows the setup for the image acquisition. The basis for image acquisition was a Sony "ILCE-6400" camera, which comes with an interchangeable lens and whose core is an CMOS sensor with 25 megapixels in a 3:2 aspect ratio. Regarding sensitivity, the photographer has ISO 100 to ISO 102,400 available [39]. The lens used is the Sony "FE50mm F1.8", which has a fixed focal length of 50 mm and apertures from $f/1.8$ to $f/22$ [40]. A foldable photo studio ("Foldio3" by Orangemonkie [41]) was used to ensure a homogeneous background. A green background was chosen for photographing ice shapes on propeller blades and airfoils, providing high contrast to the ice and the ice-covered components. LED lighting ensured sufficient and even illumination of the object of interest and practical minimization of shadows. To generate images with adequate overlap and from all sides, the camera was permanently mounted, and the object of interest was placed on a turntable ("Foldio360" by Orangemonkie [42]), which was operated via Bluetooth with the smartphone in a corresponding app. The number of images per complete turntable rotation was also set in the app. A remote IR signal for each position automatically triggered the camera.

The camera was initially mounted using a tripod and an articulated arm, which could be locked in place using several ball joints, thus offering a high degree of flexibility about the camera position. However, due to the many adjustment options, setting the exact camera position with repeat accuracy found to be insufficient. In addition, the lack of rigidity sometimes led to blurred images in the event of vibrations, as can occur in the IWT. For this reason, a frame made of aluminum profiles was designed to mount the camera, on which it could be locked using ball heads. The rack has six mounting options: three for upright shots for digitizing propeller blades and three in landscape format for capturing the airfoils. The photogrammetry course at the University of Svalbard also recommends using at least three photo haloes [17]. Once adjusted, the camera could be attached or detached within a few seconds using a quick-release system, allowing it to quickly switch between the different camera positions.

The airfoil was placed upright on a base plate, which was also printed and had a form-fitting groove for fastening. To photograph the propeller, a frame made of aluminum profiles was designed, to which the propeller was screwed against a mechanical stop. Thus, it was fixed in all six degrees of freedom. The propeller blades were photographed individually to ensure a sufficiently good resolution of the images. The camera aimed at the lower part, and the propeller was rotated. The distance between the camera rack and the turntable was set to 40 cm.

Both mounting frames were equipped with GCPs to scale and reference the later reconstructed model. The referencing process is described in more detail in the following section 3.5.
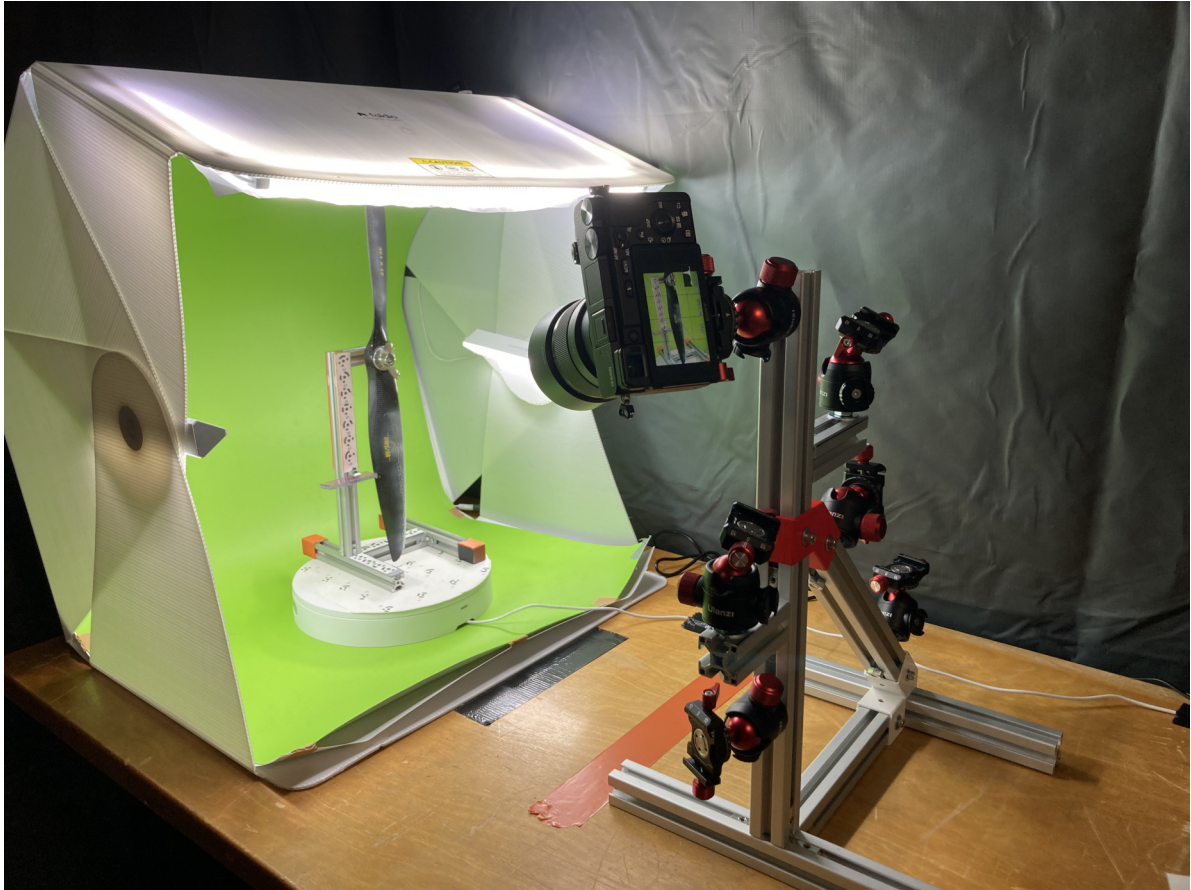
Figure 3.4: Setup for the image acquisition.

Camera Settings

Well-exposed, high-resolution photos with clearly recognizable object features form the basis for the subsequent 3D reconstruction. Therefore, it is essential to optimize the camera settings. Many cameras offer automatic mode, which delivers good results for single images. However, adjusting the camera parameters individually for each image can make the subsequent feature alignment between the images more difficult. Therefore, shooting should be done in manual mode to ensure static camera settings [17]. Manual mode allows for setting ISO, aperture, and shutter speed. The ideal combination of these three settings options for digitizing ice shapes was to be determined. The tests carried out for this purpose are described in Chapter 4. The following additional settings were used:

Focus Mode
The focus mode was also set to manual and the focus was on the ice shape. In principle,

photography in automatic mode would also be possible if the turntable's delay between movements was set long enough. However, experience showed that, especially with the propeller blades, the focus was partly on the frame, not the ice shape.

White Balance
To ensure alignment, the color temperature should be static and constant (no auto white-balance). According to Betlem, 5600 K is a good value [17].

File Type
Either unprocessed raw image format (RAW) or compressed format developed by the Joint Photographic Experts Group (JPEG) can be used as the file type for the photos. The RAW format resulted in significantly longer processing times but without observable improvements. Therefore, images were stored in the more compact JPEG format.

3.4 Photogrammetry

Once the images were taken, the actual SfM process could begin with reconstructing the 3D object from the 2D images. Various software applications are available to perform the individual steps of SfM photogrammetry, described in chapter 2.4. A commonly known tool that was also used in this thesis is the commercial Software Metashape, developed by Agisoft LLC. Metashape enables all the steps described via a user-friendly graphical user interface (GUI), from feature detection, matching, filtering tie points, calculating depth maps, and finally, creating and exporting the resulting 3D models (Figure 3.8). Metashape also offers an application programming interface (API) that allows fully automating processes using Python scripts. The University of Svalbard provides an excellent tutorial on SfM photogrammetry with Metashape [17].

The steps described below were initially carried out manually to understand the program's process and setting options. Later, the various steps were scripted in Python code to automate the entire workflow. Essential variables and filter thresholds were defined at the beginning of the script and could, therefore, be easily changed. This enabled an efficient and customizable workflow that saved much time for the progress of SfM photogrammetry and allowed parallel working during the script's execution.

Photo Alignment

In the first step, captured photos of iced blades or airfoils were uploaded to the software. Image quality was analyzed, and pictures of insufficient quality were disabled for the later alignment process. Agisoft recommends excluding images with a quality value of less than 0.5 units [23]. Only the images that meet the quality requirements were evaluated in the next steps.

The next step was to identify key points, derive feature descriptors from them, and compare them between the images. Figure 3.5 shows the features found by the software in an example image. Gray dots are determined key points, blue dots are common key points that could be found and matched in several photos, also called tie points. These tie points enable the estimation of the camera position and thus the reconstruction of the 3D scene by triangulation of the key points (see section 2.4 and Figure 3.6). Metashape summarizes this process in the "Align photos" function. The result is a is a low-density or "sparse" point cloud.
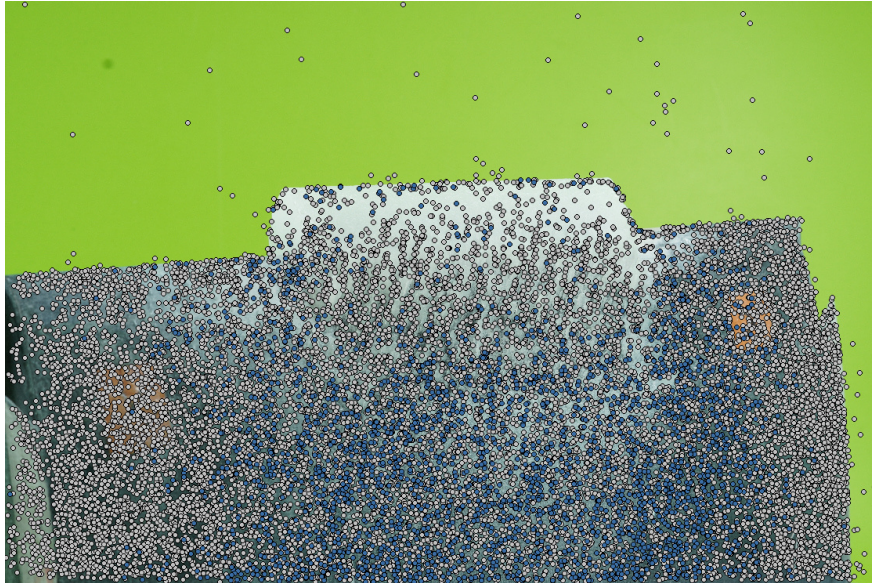
Figure 3.5: Detected key points (gray) and tie points (blue) in an example image.
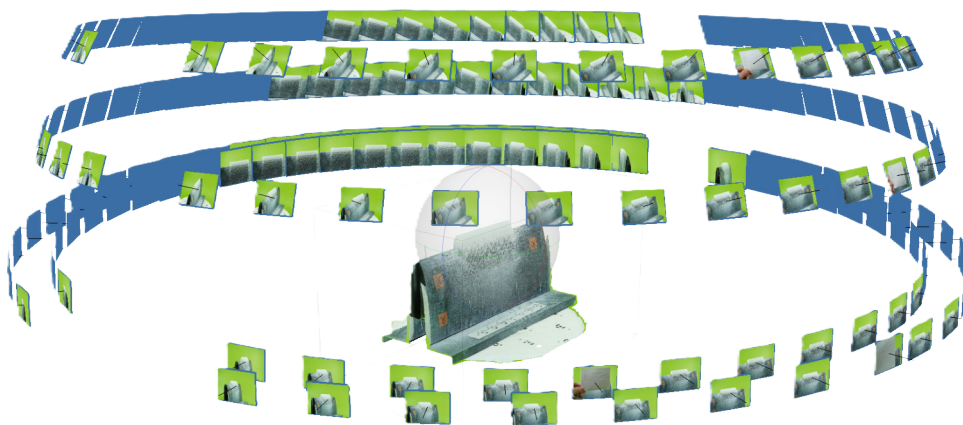
Figure 3.6: SfM enables the simultaneous reconstruction of the 3D scene and camera positions.

Error Reduction-Optimization

Before generating the final "dense" point cloud, several filtering steps were necessary to select and remove low-quality tie points and optimize the quality of the sparse cloud and the camera alignment. According to the United States Geological Survey (USGS)s' recommendations, this includes: [43]

- **Reducing the Reconstruction Uncertainty:** a numerical expression indicating the level of uncertainty in the position of a tie point. It is determined by assessing the geometric relationship of the cameras responsible for projecting or triangulating that point, considering factors such as geometry and redundancy. Mathematically, it is expressed as the ratio between the largest and smallest semiaxis of the error ellipse of the triangulated 3D point coordinates [23]. USGS recommends a threshold value for the Reconstruction Uncertainty of 10 [43].

- **Improving Projection Accuracy:** measured by the "mean key point size" which indicates the standard deviation of the Gaussian blur at the key point's identified scale. Precision increases with lower standard deviation values. Projection accuracy reflects how precisely a tie point can be determined, considering the size of the key points that converge to form it [23]. USGS's recommendation for the Projection Accuracy level is 2 [43].

- **Lower the overall Reprojection Error:** measures the disparity between a 3D point's original location on the image and the location of the point when it is projected back to each image used to estimate its position. High reprojection error indicates poor localization accuracy of the corresponding point projections at the point matching step [23]. USGS recommends here a threshold value 0.3 [43].

(a)   (b)
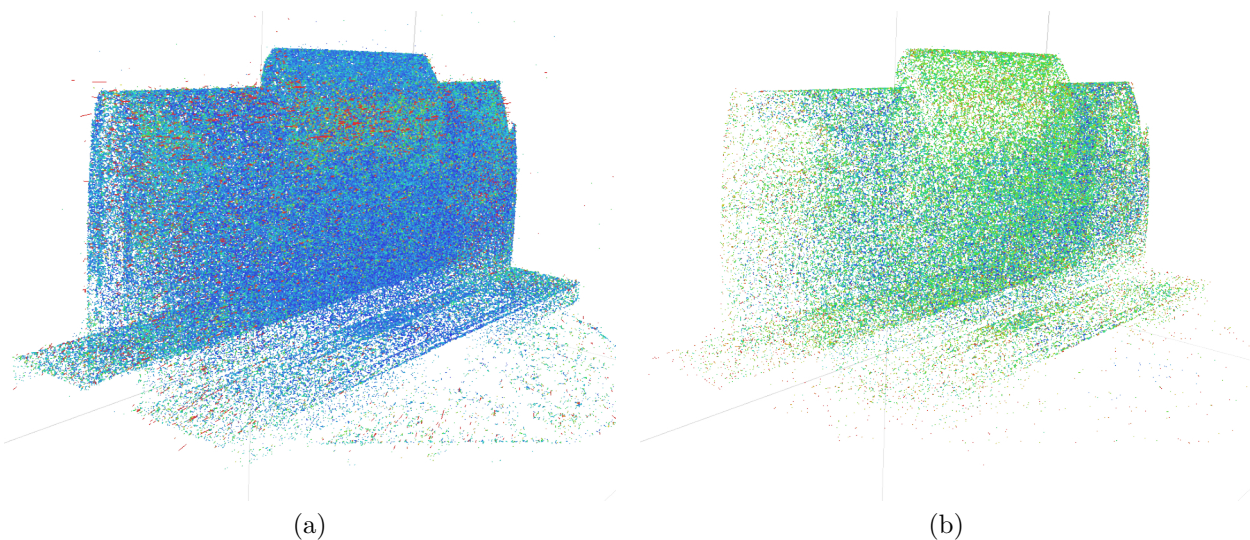
Figure 3.7: Point cloud variance of the (a) original and (b) filtered sparse point cloud. Vector length and color correlate to the magnitude of the estimated position error.

The aim of these filtering steps is to derive a sparse point cloud made up of only high-quality tie points and iteratively optimize the camera model (Figure 3.7). However, too many optimization runs may result in overfitting the data. Consequently, the model deviates from its original reliance on actual input data and instead becomes dependent on internal processing parameters [17]. Too aggressive filtering also leads to a considerable loss of information. The script has been adapted so that the threshold values for Reconstruction Uncertainty, Projection Accuracy, and Reprojection Error were iteratively increased so that a maximum of 50 % of the previous tie points were removed with each optimization step. This value is also based on the USGS recommendations [43].

Model Reconstruction

Based on the estimated and optimized camera positions in the next step a dense point cloud could be estimated by calculating depth values for every pixel in the images and, hence, depth maps for each image. Dense cloud filtering could be done to enhance the quality further according to the "point confidence". "Confidence" in this sense means how many depth maps have been used to generate each dense cloud point [23]. For the final 3D mesh, dense point cloud estimation was optional.

Metashape can reconstruct a polygonal mesh model based on point cloud information or depth map data. For arbitrary surface reconstruction, Agisoft recommends the depth maps setting, which more effectively uses all the information from the input images and is less resource-demanding than dense cloud-based reconstruction [23]. Reconstruction from dense point cloud data might be helpful for externally imported dense point cloud data or for planar surfaces, such as terrains; however, it proved less suitable for modeling ice shapes.

(a)   (b)   (c)
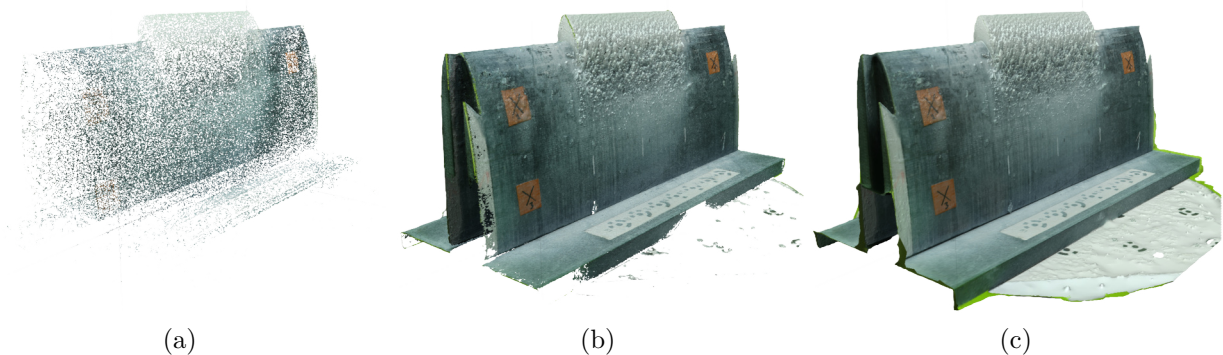
Figure 3.8: (a) Sparse point cloud, (b) dense point cloud and (c) meshed 3D model reconstructed with Agisoft Metashape.

The finished result could then be textured or exported directly. Metashape offers various formats for exporting 3D models [23]. However, since no information about color or texture was required for the evaluation, an export as an stereolithography (STL) could be done.

3.5 Referencing and Scaling

For the reconstructed 3D model to be evaluated and analyzed, it needed to be scaled and referenced. In the past, this was done manually in a time-consuming process using CAD programs. Therefore, the referencing should be done automatically within the reconstruction process in Metashape. Based on GCPs in the form of coded markers with known coordinates, th model could be scaled and transferred to a defined coordinate system. Conveniently, Metashape creates its own markers of the type Schneider circular coded target (see Figure 2.7(a)). Those targets were automatically detected by the internal image recognition software and assigned to the model.

Marker Attachment

The targets were printed on non-reflective textured paper and attached to the propeller's frame or the airfoil base plate. They had to be accessible to measure and visible on the images. Attaching the markers to the frame instead of directly to the aerodynamic surface had two significant advantages: First, the targets only needed to be attached once, not for each series of measurements. Instead, the measurement object was replaced. A joint coordinate system could be assumed as the measurement object could not move in relation to the frame. Second, the mounting frames' cubic shape allowed for a much more precise manual measurement than the blades or airfoils' curved surfaces.

Marker Detection and Coordinate Assignment

An initial coordinate system was first determined to define the object's pose and scale. An initial origin needed to be assumed from which the positions of the markers were measured. This can, for example, be a corner of the frame or one of the markers itself. The coordinates of the fiducial markers were saved with their index or label in a comma-separated values (CSV) file in 'XYZ' format. With the "detectMarkers()" command, Metashape offers a function for automatically recognizing its markers in images, including their coding (Figure 3.9). During 3D reconstruction, these markers were assigned to the model at the corresponding position. The CSV file with the target coordinates could then be imported into the program and transferred to the markers according to their coded index. Experience showed that this step should only be carried out after the alignment; otherwise, the model was overdetermined by the already assigned coordinates. In particular, for the propeller blades, this led to alignment problems and significantly poorer results.
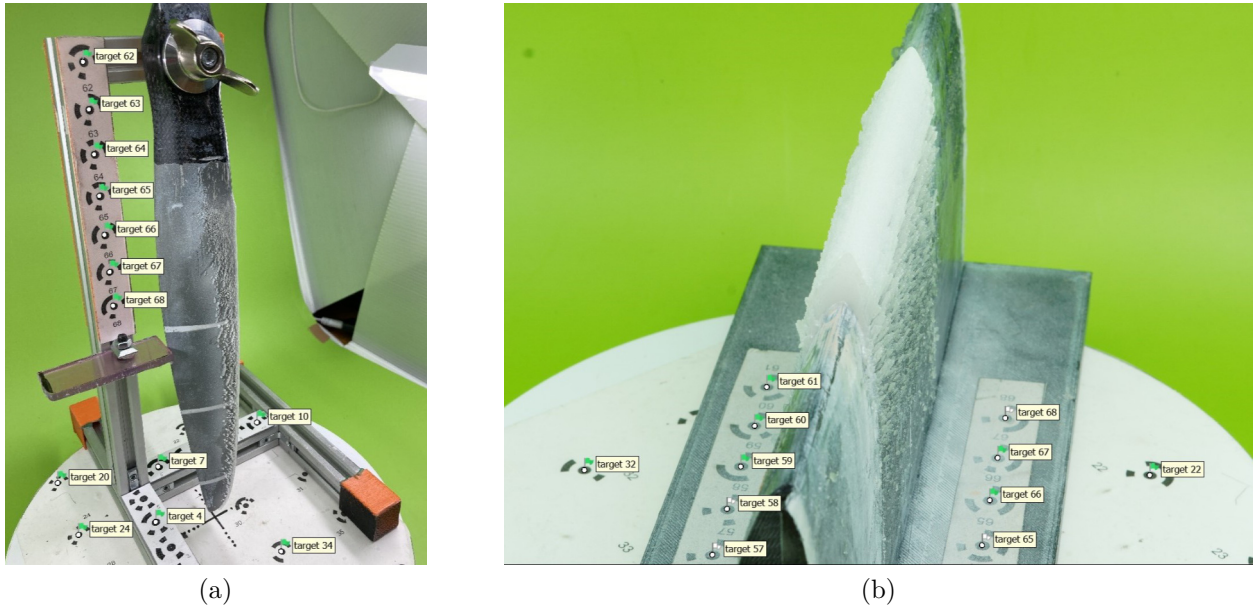
Figure 3.9: Detected markers on the photos of (a) the propeller blade and (b) the airfoil.

Reference Alignment

By assigning the real coordinates to the coded markers, the model was scaled by the distance between them and referenced by the inertially defined coordinate system. To evaluate the ice accretion, it the model needed to be compared with the original geometry as a reference. This is usually defined using a different coordinate system. Therefore, a coordinate transformation of the original inertial coordinate system into the reference coordinate system was carried out. As the model was already scaled, this was done using a rigid body transformation. Considering a geometric object modeled as a set of points in 3D space, a rigid body transform is a geometric transformation of these points that preserves the distances between them. [44].

Rigid body transformations are mathematically represented by transformation matrices. Each point $\underline{P}$ of the modeled object can be transferred to $\underline{P'}$ by multiplying its coordinates with the transformation matrix $\underline{\underline{T}}$ [45]:

$$\underline{P'} = \underline{\underline{T}} \cdot \underline{P} = \underline{\underline{T}} \cdot \begin{bmatrix} P_x \\ P_y \\ P_z \end{bmatrix} \tag{3.1}$$

The transformation matrix $\underline{\underline{T}}$ for 3D rigid body transformation is defined as [45]:

$$\underline{\underline{T}} = \begin{bmatrix} \underline{\underline{R}} & \underline{d} \\ \underline{0} & 1 \end{bmatrix}, \ \underline{\underline{R}} \in SO(3), \ \underline{d} \in \mathbb{R}^3 \tag{3.2}$$

where the sub-matrix R defines the rotation part of the transform, and the translation vector d representing displacement in 3D space [45]:

$$\underline{d} = \begin{bmatrix} d_x \\ d_y \\ d_z \end{bmatrix} \tag{3.3}$$

A standard method of specifying a rotation matrix is its description as a product of successive rotations about the principal coordinate axes x, y, and z. In the aviation standards (German aviation standard DIN 9300, international standard ISO 1151-1), these individual rotations are stated as [46]:

- roll angle ϕ (around the x-axis)

- pitch angle θ (around the y-axis)

- yaw angle ψ (around the z-axis)

The basic rotation matrices are defined as [45]:

$$\underline{\underline{R_x}}(\phi) = \begin{bmatrix} 1 & 0 & 0 \\ 0 & \cos(\phi) & -\sin(\phi) \\ 0 & \sin(\phi) & \cos(\phi) \end{bmatrix} \tag{3.4}$$

$$\underline{\underline{R_y}}(\theta) = \begin{bmatrix} \cos(\theta) & 0 & \sin(\theta) \\ 0 & 1 & 0 \\ -\sin(\theta) & 0 & \cos(\theta) \end{bmatrix} \tag{3.5}$$

$$\underline{\underline{R_z}}(\psi) = \begin{bmatrix} \cos(\psi) & -\sin(\psi) & 0 \\ \sin(\psi) & \cos(\psi) & 0 \\ 0 & 0 & 1 \end{bmatrix} \tag{3.6}$$

The compound rotation matrix is obtained by multiplying the matrices of the individual rotations. However, rotations are generally not commutative, meaning different rotation sequences lead to other transformations. Rotations can be described as active or passive movements. Active transformation directly changes a point's coordinates, while passive transformation changes the coordinate system itself, leaving the point unchanged. Since the coordinate system is adjusted (not the object fixed in virtual space), only the passive rotation is of significance here. The aviation standard DIN 9300, which also defines passive transformation matrices, specifies the order of rotation as $'z - y - x'$, i.e. first yawing by z through an angle ψ, then pitching by y through an angle θ and finally rolling by x through an angle ϕ [46]. The resulting rotation matrix is thus given as [45]:

$$\underline{\underline{R}} = \underline{\underline{R_z}}(\psi) \cdot \underline{\underline{R_y}}(\theta) \cdot \underline{\underline{R_x}}(\phi) \tag{3.7}$$

Furthermore, a distinction must be made between intrinsic and extrinsic transformations. With intrinsic rotations, the rotations are described relative to the coordinate axes of the

rotating object itself. Vice versa for extrinsic rotations, the rotations are defined relative to a fixed reference or global coordinate system. Thus, the individual matrices are premultiplied by each other, or in other words, the rotation sequences shift to $'x - y - z'$ to obtain the desired rotation matrix [45]. However, for this case, assuming that the SfM model is aligned with a reference model (e.g. a CAD component), it is rotated and shifted relative to its own coordinate axes (Figure 3.10). Thus, an intrinsic rotation can be assumed, and the rotation sequence corresponds to equation (3.7).
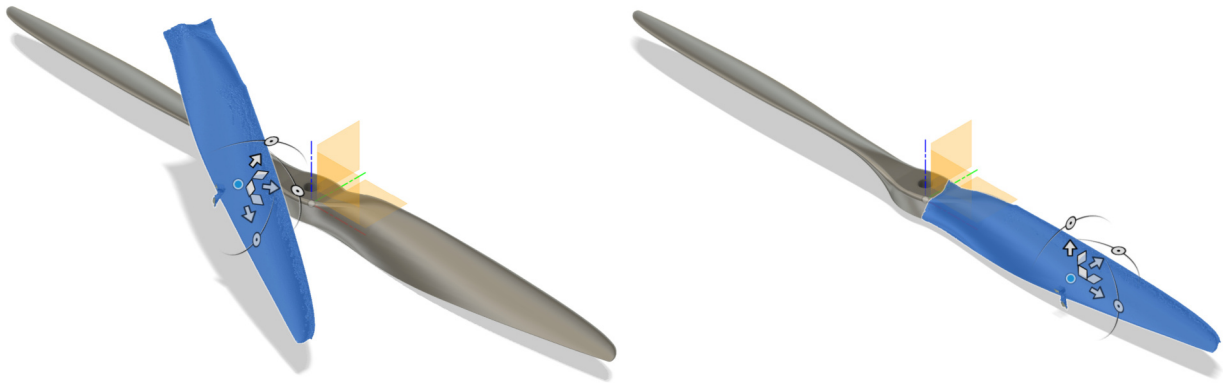
Figure 3.10: Alignment of the reconstructed model to the reference body can be done by rotation and translation around its coordinate axes.

A script was developed that used the described steps to transfer the coordinates of the markers stored in the CSV file to the reference coordinate system. The new coordinates could then be re-imported into the photogrammetry program, and the model and all future measurement series with the same geometry were now aligned with the reference geometry. The values for the rotation angles ϕ, θ, and ψ and translations in x, y, and z had to be determined once, e.g. by using a CAD program. All further test series automatically aligned with the reference coordinate system if the geometry remained the same.

3.6 Post-Processing

The preceding steps outline the process of acquiring a digital model of the ice accretion test from experiments conducted in IWTs. However, the evaluation and analysis of this data is an essential part of the methodology used to conclude the experiments. Within the UAV Icing Lab, various options exist for conducting this evaluation, some of which are supported by pre-existing scripts and processes. The ice accretion experiments primarily serve as a basis and reference for validating CFD simulation models. These usually provide results from 2D cross-sections, which is why many of the following evaluations also refer to the 2D cross-section of the propeller blades or the airfoil. The following section outlines several methods for visual and statistical evaluation of the digitized ice shapes.

Ice Contour Plot

A simple method of visualizing ice accretion is to display it as a two-dimensional ice contour plot over the clean geometry. The visualization and analysis software tool Tecplot allows for extracting and plotting 2D coordinates for certain cross sections from the generated STL file [47]. This methodology enables a straightforward and efficient comparison of the iced geometry with the reference profile but does not provide any information on three-dimensional features.
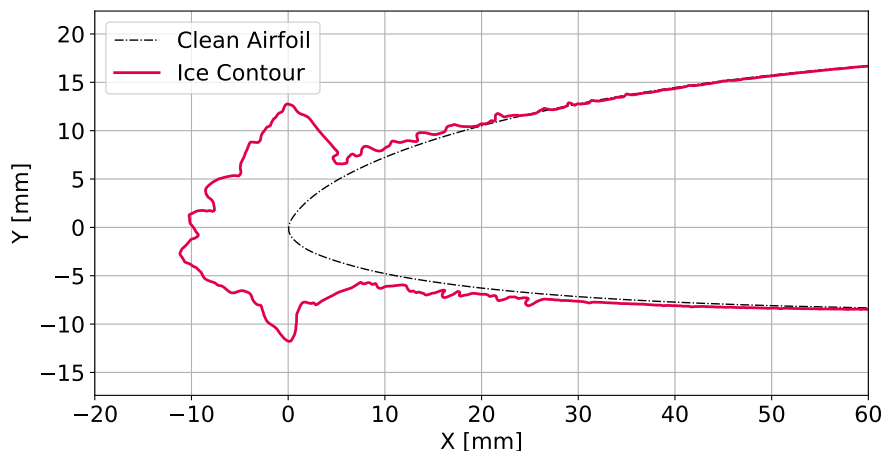
Figure 3.11: Contour plot of glaze ice accretion.

Maximum Combined Cross Section

Many ice accretions have highly three-dimensional morphological features, so a 2D description is rarely adequate. However, most icing simulation tools provide 2D cross-sections of the iced geometry. The Ohio Aerospace Institute presented an approach in which several cross-sections with defined spacings are taken, covering a specific span around a particular wing span position [48]. These cross-sections are then projected into a single plane, and the maximum outline is determined (Figure 3.12). The maximum combined cross section (MCCS), therefore, represents the outermost extent of the ice accretion over the defined span distance. This enables 3D features to be captured and visualized over a specific range.

The number of cross-sections and their spacing to each other or the cross-section of interest were defined in a script. Tecplot extracts these cross-sections at the specified points and subsequently superimposes them. The result is a set of points in the euclinical plane. The concept of the alpha shape was applied to create a bounding area that envelops these points. The alpha shape is a geometric concept used to generalize bounding polygons containing sets of points. The alpha shape is defined based on a parameter α. For a given set of points, the alpha shape includes only those parts of the convex hull of the points that have a diameter smaller than α. In simpler terms, it captures the concave parts of the
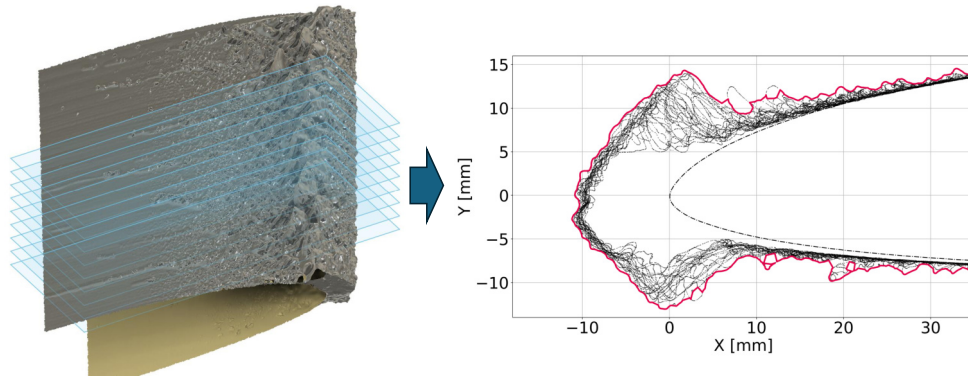
Figure 3.12: Schematics of the process to obtain the MCCS of a 3D scanned ice shape.

shape formed by the points. The convex hull, a shape similar to what you would see if you wrapped a rubber band around pegs at all data points, is an alpha shape where the alpha parameter is zero [49]. By adjusting α, more details, such as ice feathers, can be captured, but features can also get lost (Figure 3.13). Values for α between 2 and 4 have proven to be reasonable. The number of cuts required within the defined span for the cross-sectional area to converge was examined and is presented in Chapter 4.

(a)

(b)
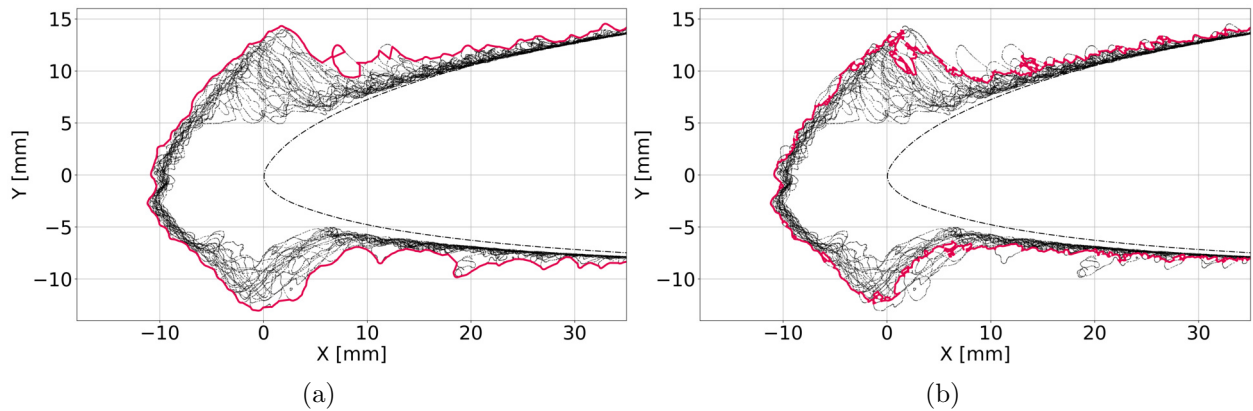
Figure 3.13: Influence of the parameter α on the shape of the MCCS. Alpha shape generated with (a) $\alpha = 1.5$ and (b) $\alpha = 8$.

To apply the MCCS to swept airfoils, a correction parameter Δx was defined to shift the leading edge point of all cross-sections along x to $x = 0$. The correction parameter for a sweep angle φ for a distance Δz in the spanwise direction from the coordinate origin is defined as:

$$\Delta x = \Delta z \cdot tan(\varphi) \tag{3.8}$$

Ice Thickness, Volume, and Density

The statistical analysis of ice thickness is a standard method in icing studies. On the one hand, it is used to validate simulation codes [4], and on the other hand, the ice thickness or the iced cross-sectional area can be used to determine the volume and density. The ice thickness extraction was performed by unwrapping the digital model along the surface of the clean airfoil as reference geometry. Consequently, the coordinate systems changed from $X - Y$ to $S - D$, whereas S describes the surface coordinate and D describes the ice thickness. In this new system, the airfoil is positioned at $D = 0$, while $S = 0$ aligns with the stagnation point of the pristine airfoil (Figure 3.14).

The cross-sectional area of the ice can be determined by integrating the thickness over the unwrapped distance S (Figure 3.15). If the areas A_i of several cross sections are integrated at the point z_i along the span coordinate Z, the volume V over these areas is approximated. Using the trapezoidal rule, the formula for this is

$$V = \sum_{i=1}^{n} \frac{1}{2}(A_i + A_{i-1}) * (z_i - z_{i-1}) \tag{3.9}$$

where n is the number of cross sections. The trapezoidal rule is a technique for numerical integration, i.e., approximating the definite integral. The greater the number n of cross-sections, the more accurately the volume is determined. In Chapter 4, the number of cross-sections required for the volume to converge was examined. The density ρ of the ice was determined by dividing its mass by volume. The mass of the ice was determined by weighing before and after testing and subtracting the iced geometry from the clean geometry.
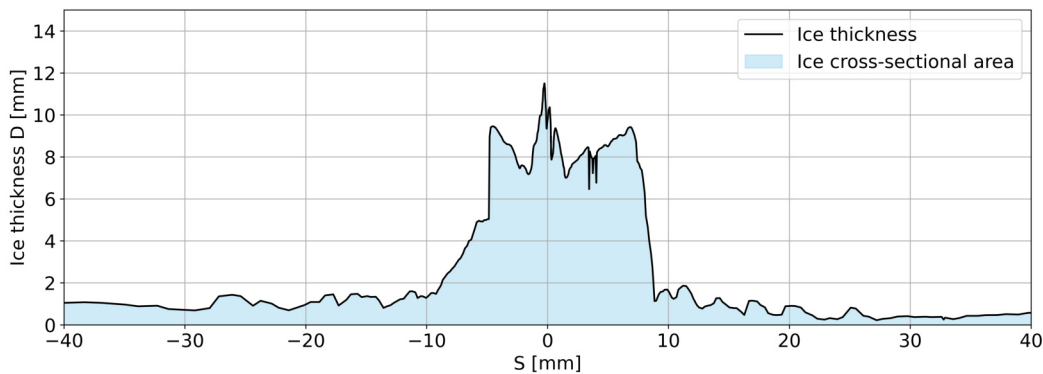
Figure 3.14: Unwrapped ice shape in the $S - D$ coordinate system
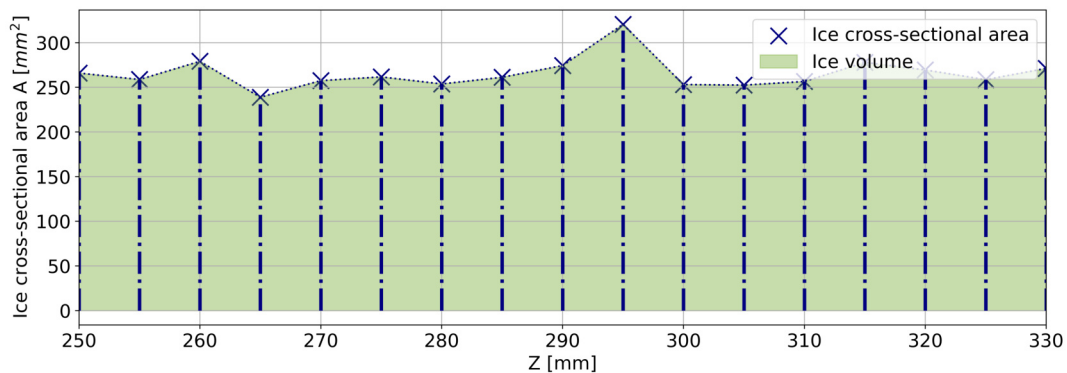
Figure 3.15: The ice volume can be approximated by integrating the cross-sectional area along the span coordinate Z.

3D Mesh Comparison

One way to visualize the thickness of the ice layer in three dimensions is a 3D contour plot based on a mesh comparison. The Hausdorff distance can be used to measure the difference between two meshes, which quantifies the maximum distance from a point in one set to the nearest point in the other set [50]. The Hausdorff distance between two layers is computed by sampling one of the two layers and, for each sample, finding the closest point over the other mesh. The mesh of interest can then be colored based on the calculated values (Figure 3.16). A suitable tool for this three-dimensional representation is, for example, the open-source mesh processing software MeshLab [51].
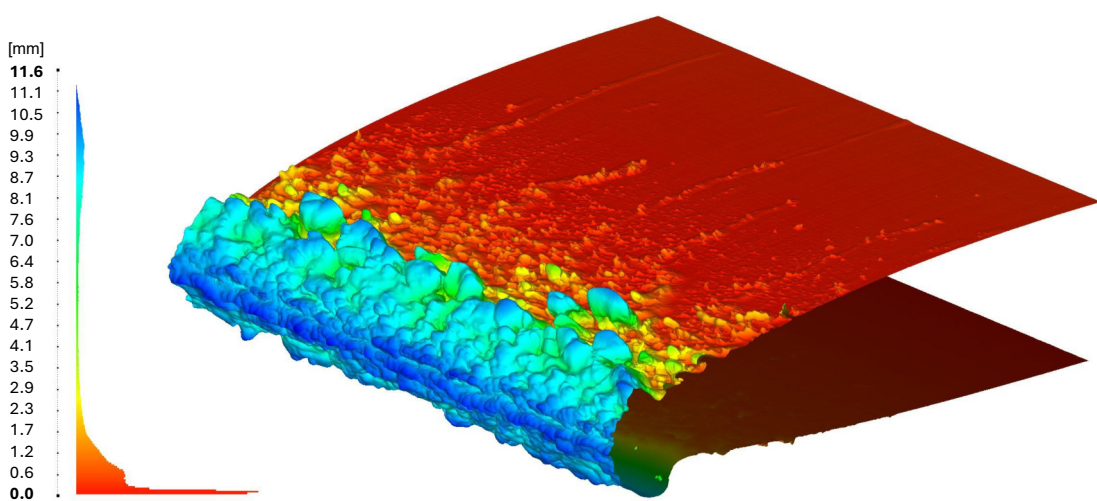
Figure 3.16: 3D mesh comparison visualizing the ice thickness on an airfoil.

Beta Distribution

Calculating the Hausdorff distances between two meshes is also a suitable approach for validating the method and asses its accuracy by comparing a known reference geometry with its SfM reconstruction. To facilitate statistical analysis, for example, to calculate an expected value, the real distribution of deviations can be approximated as a continuous probability function. For this purpose, the beta distribution can be used. It belongs to the continuous probability distributions and is parametrized by the two parameters α and β. Compared to a normal distribution, the beta probability density function (PDF) can also have boundary maxima, which increases the flexibility regarding the approximation of real distributions (Figure 3.17) [52]. The equation of the beta PDF is [52]:

$$f(t; \alpha, \beta) = \frac{\Gamma(\alpha + \beta)}{\Gamma(\alpha)\Gamma(\beta)} t^{\alpha-1} (1-t)^{\beta-1} \tag{3.10}$$

based on the gamma function [52]:

$$\Gamma(t) \equiv \int_0^\infty x^{t-1} e^{-x} \, dx \tag{3.11}$$

The expected value of the beta distribution is calculated as [52]:

$$E[X] = \frac{\alpha}{\alpha + \beta} \tag{3.12}$$
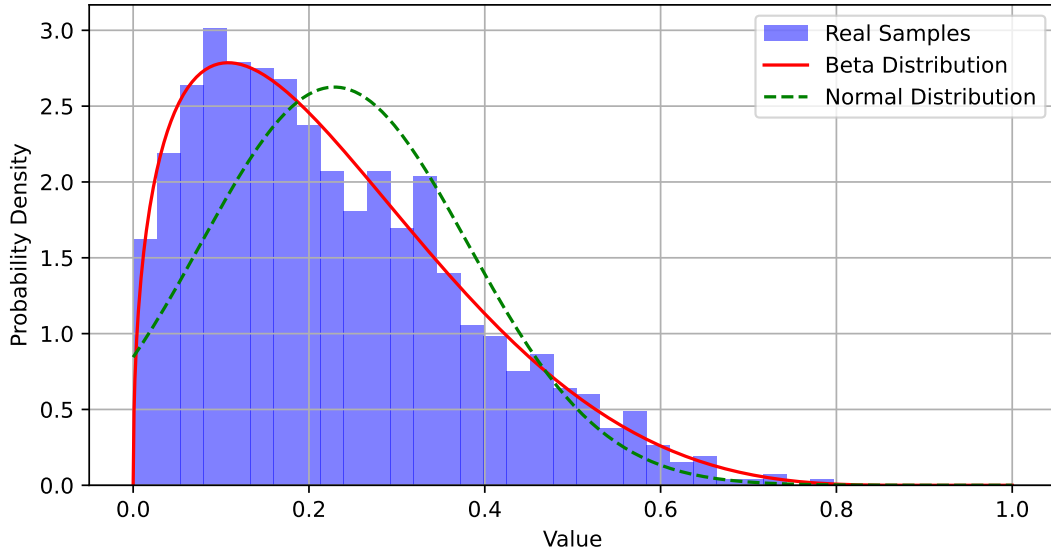
Figure 3.17: Approximation of real distribution: Beta vs. Normal distribution

4 Testing

The tests carried out during this thesis can be divided into three categories. First, the method was applied and validated in an IWT test campaign under field conditions. Second, tests were conducted to determine and evaluate the method's accuracy. Lastly, further tests were done to refine and optimize the method and parameters.

4.1 Validation

The developed process of digitizing ice shapes via SfM photogrammetry was applied and tested during an IWT test campaign at the VTT in Helsinki. The aim was firstly to validate the methodology under natural conditions with actual ice accretion and secondly to investigate whether and where there was still potential for improvement. Various icing scenarios were to be tested for both propeller blades and airfoils. The experiments were carried out in collaboration with other projects, so their investigations were primarily at the forefront, and their evaluation was to be carried out using photogrammetry.

Table 4.1 lists the test runs for ice accretion on airfoils. The airfoil type was RG-15 8.9% and was tested as an unswept and swept geometry with a sweep angle of 20°. For reasons of redundancy, two test runs were carried out for each of the two airfoil types at temperatures of -10 °C (rime ice), -4 °C (mixed ice) and -2 °C (glaze ice). All other parameters were kept constant.

Table 4.2 details the test runs for ice accretion on propeller blades. The propeller diameter was 21" and the pitch was 13". Seven test runs were carried out, varying the duration of the icing conditions, revolutions per minute (RPM), and LWC. However, due to technical problems with the propeller test rig, tests could only be conducted at -10 °C under rime ice conditions.

Table 4.1: Test parameters for ice accretion tests on airfoils.

Run	Type	Temperature [°C]	Speed [$\mathrm{m\,s^{-1}}$]	LWC [$\mathrm{g\,m^{-3}}$]	Duration [min]
15	RG15	-10	25	0.52	20
16	RG15	-10	25	0.52	20
29	RG15	-4	25	0.52	20
30	RG15	-4	25	0.52	20
31	RG15-Swept	-4	25	0.52	20
32	RG15-Swept	-4	25	0.52	20
42	RG15	-2	25	0.52	20
43	RG15	-2	25	0.52	20
71	RG15-Swept	-10	25	0.52	20
72	RG15-Swept	-10	25	0.52	20
97	RG15-Swept	-2	25	0.52	20
98	RG15-Swept	-2	25	0.52	20

Table 4.2: Test parameters for ice accretion tests on propeller blades.

Run	Type	Temperature [°C]	Speed [$\mathrm{m\,s^{-1}}$]	LWC [$\mathrm{g\,m^{-3}}$]	Duration [s]	RPM [$\mathrm{min^{-1}}$]
111	21x13	-10	25	0.42	60	4200
112	21x13	-10	25	0.42	60	4200
113	21x13	-10	25	0.42	60	4200
130	21x13	-10	25	0.42	600	4200
131	21x13	-10	25	0.42	60	4620
132	21x13	-10	25	0.42	60	3780
133	21x13	-10	25	0.24	95	4200

4.2 Accuracy Assessment

In addition to developing the photogrammetry method for digitizing ice shapes, this thesis's second aim was to analyze and evaluate the output quality. The second section, therefore, deals with tests to verify the method's accuracy. First, the size of features the method can still recognize and digitize should be examined. Second, the methodology's accuracy in reconstructing a known geometry should be investigated; in other words, how good the digital copy of the known geometry is. Third, the method's accuracy in referencing the 3D model and, thus, the repeatability of its pose.

Minimal Resolvable Feature Size

This test aimed to determine the minimum possible feature size that the developed method can capture. For this purpose, a benchmark specimen was designed and produced by fused filament fabrication (FFF) 3D printing. It was then digitized using SfM. The specimen had different sizes of artificial roughness in the form of pyramids with a height of 0.2 mm - 0.5 mm (Figure 4.1(a)). The three-dimensional reconstruction of this specimen should show to which size of the pyramids is still recognizable.

Initially, this test should be repeated with the same geometry as an ice shape (Figure 4.1(b)). A silicone mold was developed for this purpose, and the ice shape was produced by filling it with water and putting it into the freezer. However, due to the water's surface tension, the pyramids' peaks were not completely filled. Even adding surfactants such as washing-up liquid did not significantly improve the ice shape. Therefore, it was decided not to pursue the second approach any further.

(a) (b)
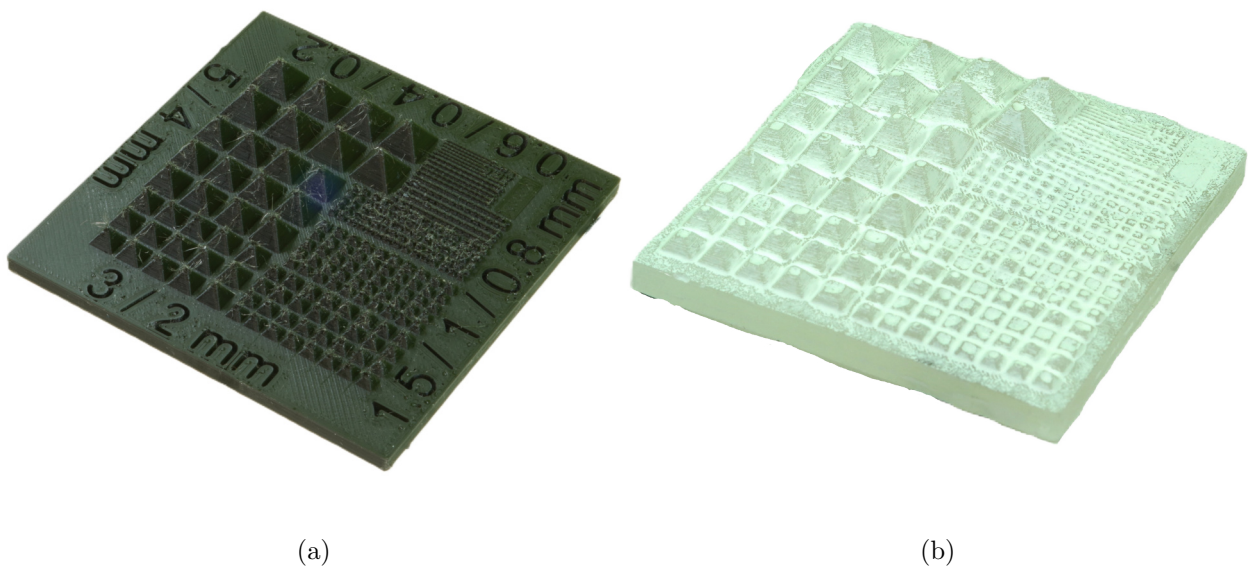
Figure 4.1: Benchmark specimen with artifical roughness to determine the minimum possible feature size that photogrammetry can capture. (a) 3D printed and (b) casted and colored ice shape.

Accuracy Measurement based on a Known Geometry

This test deals with the accuracy of 3D reconstruction. For this purpose, a known geometry was reconstructed, and the SfM digitized copy was compared with the original. To demonstrate a case as close to reality as possible, the 3D print of an ice shape on an airfoil previously digitized using photogrammetry served as the test object. The specimen, otherwise used for presentation purposes, was produced using the selective laser sintering (SLS) process, so a high production quality and a negligible manufacturing error can be assumed. The reconstructed SfM model was then aligned with the original CAD file as a reference to determine the deviation of the two meshes and, thus, the reconstruction error.
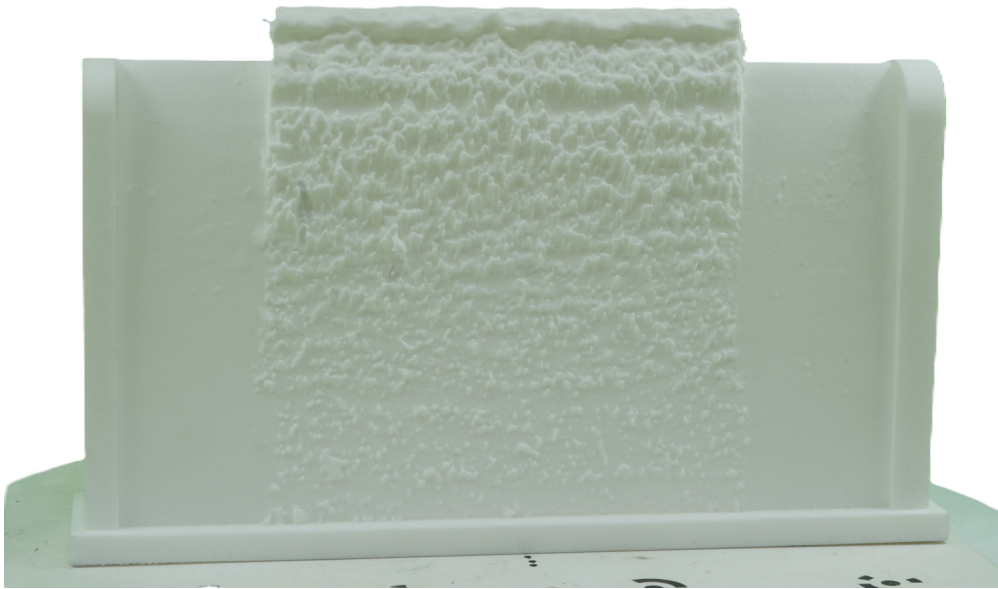
Figure 4.2: 3D printed known geometry as reference object for the accuracy measurement.

Repeatability of the Object's Pose

In addition to the accuracy of the 3D reconstruction itself, examining the repeatability of the object's pose makes sense. Possible sources of error are:

1. Positioning errors when mounting the geometry in the holding frame.

2. Positioning errors during SfM reconstruction, for example, due to incorrect alignment.

3. Positioning errors during the referencing process, for example, during marker recognition and assignment.

As the the propeller blades were screwed in and thus tensioned, it can be assumed that the positioning error during mounting is negligible (This does not necessarily apply to the

airfoil, since it needed some tolerance to fit into the groove of the base plate). The error caused by photogrammetry was examined in the previous test. This leaves the investigation of the repeatability of the referencing.

For this purpose, the method described above was repeatedly applied to a propeller blade. A total of three photosets were taken (without de-mounting the propeller), which were analyzed independently of each other using photogrammetry. The rotation angles and distances for the reference alignment were determined manually in the CAD program for the first dataset, and the transformed coordinates were assigned to the individual models. Therefore, their markers were given the exact coordinates, and the models, based on the different photosets, were compared with each other.

4.3 Further Method Refinement

Methodology development is an iterative process that requires extensive testing. This chapter briefly describes the most important experiments to further refine and optimize the abovementioned methodology.

Optimization of the Camera Parameters

Photogrammetry is based on well-exposed, high-resolution photos with clearly recognizable object features. Three settings primarily influence the quality of the images: ISO sensitivity, aperture, and exposure. These are directly linked to each other, so finding an optimum between the three adjustments is crucial. A non-iced airfoil geometry was initially used as a test object. The tests were later repeated in the IWT with ice accretion on the airfoils.

The experiments were divided into two parts to find the optimal camera settings. First, the airfoil was photographed with different aperture sizes and ISO values. The shutter speed was adjusted according to the rule of equivalent exposure so that the exposure remained constant in each case (see Figure 2.8). Aperture settings were tested with f-stop settings of $f/8 - 22$ at an ISO sensitivity of ISO 100, ISO 200, ISO 400, and ISO 800. Second, a similar series of tests was undertaken. However, this time, the ISO and aperture were kept constant (ISO 100 and $f/13$), and the exposure increased gradually. Images were taken at various shutter speeds from 1/10 s to 0.8 s. Only 36 photos from a single angle were taken to save processing time. The scene was then reconstructed for each case using photogrammetry. The number of tie points, i.e., the common features found in the images, should serve as a quality criterion for the input data since they form the basis of the 3D reconstruction (see Figure 2.5).

Image Acquisition: Smartphone vs. Professional Camera

A professional camera offers a wide range of setting options, so taking high-quality pictures requires some experience and knowledge of photography. However, taking photos with a standard smartphone is much easier. It comes with numerous tools and algorithms to quickly and efficiently generate good pictures. A smartphone would simplify the image acquisition process, especially for inexperienced photographers. Therefore, the SfM results based on photos taken with a conventional smartphone should be compared with those taken with a professional camera to test whether a smartphone camera suits the task. The smartphone tested is the iPhone SE (2nd generation) by Apple, which has a 12-megapixel camera with a single lens and an aperture of $f/1.8$ [53].

Images were captured in the same setting using both a smartphone and a professional camera. In total, 144 images were taken, 48 each from three different angles (three halos around the object). The roughness specimen (Figure 4.1(a)) was again used as test object.

Number of Cross Sections for Representative MCCS

The principle of the MCCS consists of projecting several cross-sections over a specific span onto a plane and determining the maximum envelope as stated in section 3.6. When using more cross-sections, more details are captured, but at the expense of computing time. These investigations were intended to show whether and for how many section cuts the resulting cross-sectional area of the MCCS converges. For this purpose, spans of 20, 40, and 80 mm were defined over the ice accretion, and the number of section cuts was gradually increased. Based on the number of cross-sections, the cross-sectional area of the resulting polygon envelopes was calculated and documented. The test was carried out for glaze, mixed, and rime ice.

Number of Cross Sections for Representative Ice Volume and Density

The volume and density of the ice are obtained by integrating the cross sections according to the trapezoidal rule and adding up the individual integrals. This method is a numerical approximation whose accuracy increases with the number of cross-sections. Therefore, it should be investigated whether and how many section cuts are required for the volume to converge. The ice was trimmed to about 100 mm along the leading edge, photographed and digitized using SfM. The ice volume and density were then determined using the method described in section 3.6. The outermost boundaries were placed slightly outside the ice accretion so that the entire volume was captured. The number of cross sections was iteratively increased and the calculated volume and density were documented. The values were compared with those from literature. The evaluation was carried out again for all three ice types.

5 Results

This chapter presents the results of the abovementioned tests and investigations. The structure follows that of the previous Chapter 4 so that the results from the IWT test campaign are presented first, followed by the evaluation of the reconstruction accuracy and, finally, the investigations for refining and optimizing the developed method.

5.1 Validation

This section briefly examines the qualitative results of the IWT test campaign. The aim was to digitize the ice shapes of various ice accretion tests to validate the developed method. Tests were carried out on both airfoils and propeller blades. Figure 5.1 shows some 3D models that were reconstructed using photogrammetry. The digitized ice shapes show a high level of detail and good quality. Even small details, such as ice feathers on rime ice, are clearly visible. Due to ice shedding, the ice shapes on the propeller blades are much more delicate but could also be captured well.

Figures 5.2 and 5.3 show the referenced cross-sections of the ice-accreted airfoils and propeller blades from various test runs as contour plots. The black dash-dot line shows the original CAD geometry. The models of the same geometry obtained the exact coordinates, which were determined by a single alignment. All models were scaled correctly to their physical size. Referencing was also possible, though less precisely in some cases. In the airfoil tests (Figure 5.2), Run 15 shows a slight angle offset around the z-axis. All other contours lie almost exactly on the clean airfoil. It is possible that the airfoil was not inserted correctly into its base plate. The contours of the propeller blades (Figure 5.3) could also be referenced reasonably accurately. Moving outwards along the propeller radius, however, they show slight offsets to the clean blade. This indicates that the model's coordinate system has a slight angular offset around the x-axis to that of the original geometry.

(a)

(b)

(c)

(d)

(e)
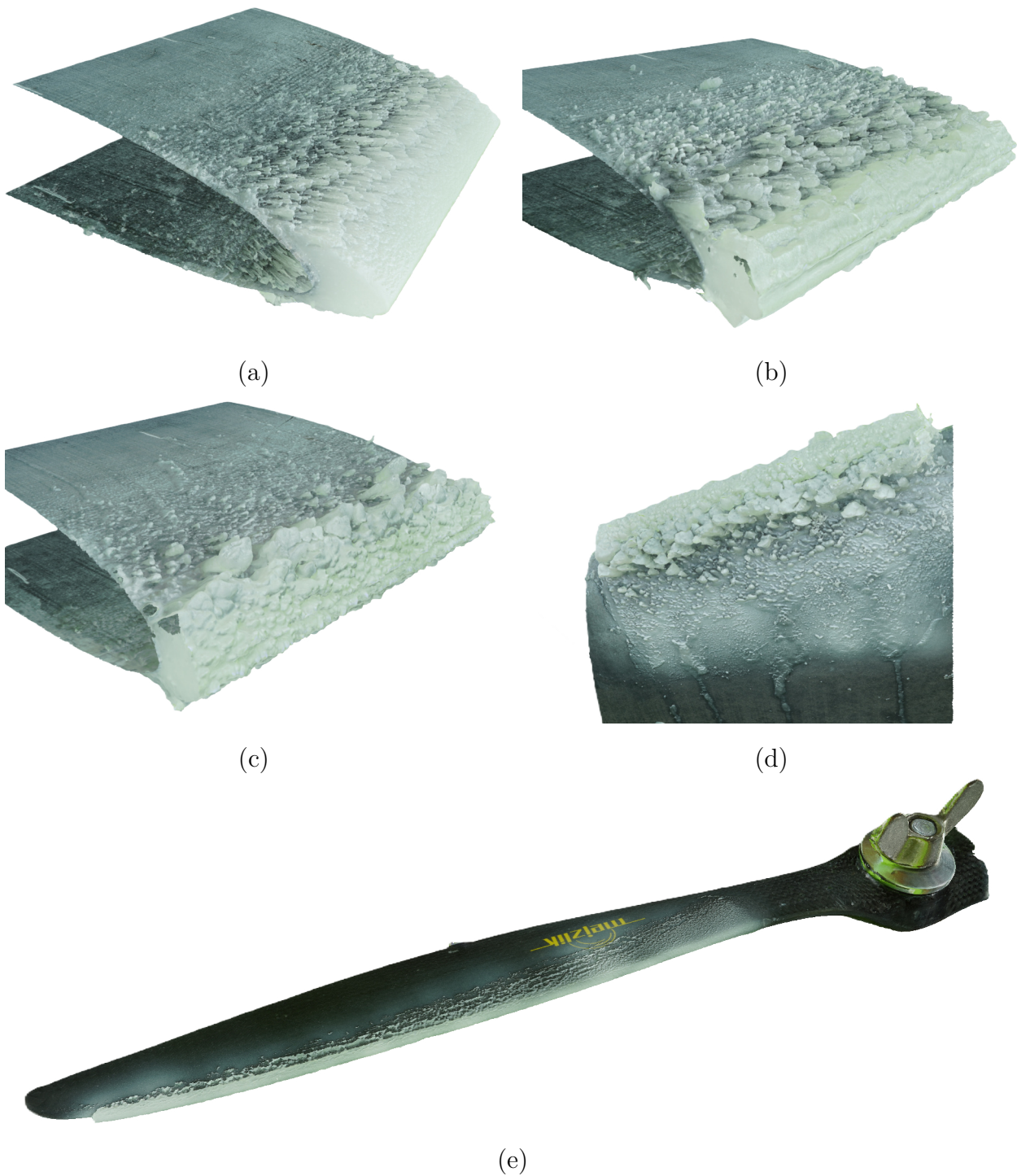
Figure 5.1: Digitized ice shapes from the IWT test campaing: (a) Rime ice, (b) mixed ice,
and (c) glaze ice on an unswept airfoil, (d) glaze ice on a swept airfoil, and (e)
rime ice on a propeller blade.
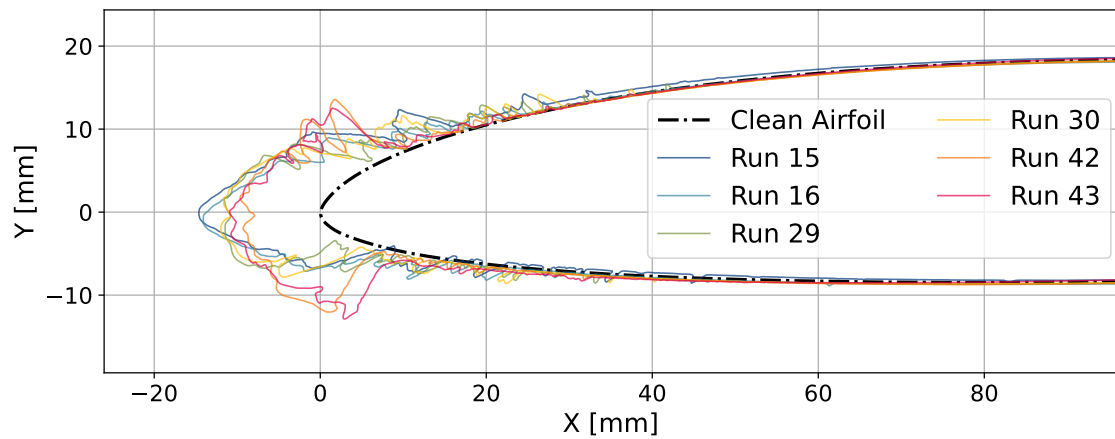
Figure 5.2: Cross-sections of ice-accreted airfoils from various test runs.
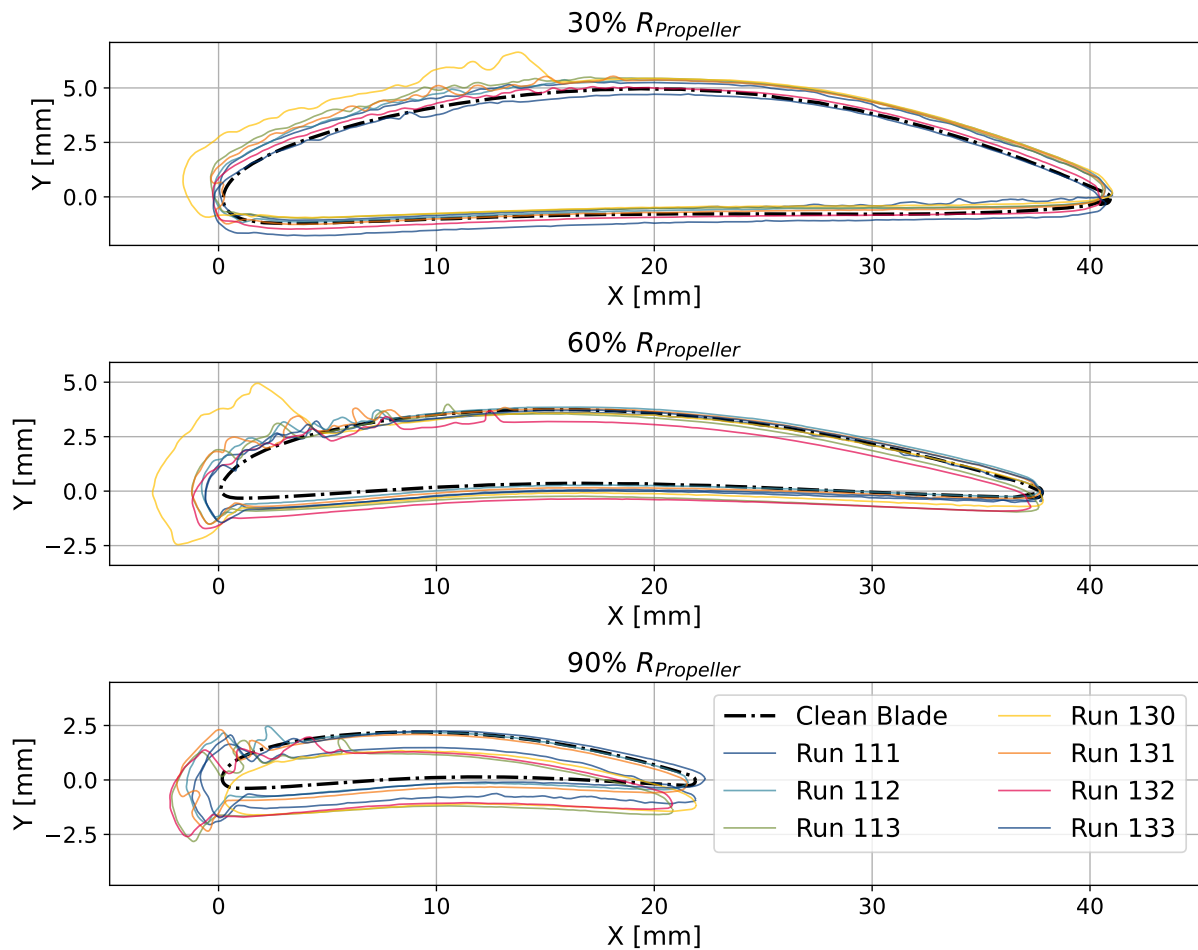
Figure 5.3: Cross-sections of ice-accreted propeller blades from various test runs at 30 %, 60 %, and 90 % of the propeller radius.

5.2 Accuracy Assessment

This section presents the results of the experiments for the accuracy assessment.

Minimal Resolvable Feature Size

To determine the minimum feature size, a geometry with artificial pyramids with a size of 0.2 - 5 mm was digitized using SfM photogrammetry. The result is shown in Figure 5.4(b). It can be seen that even fine geometries up to 0.4 mm were reconstructed well. Only the smallest size of 0.2 mm is no longer recognizable. With smaller feature sizes, the contours appear to blur. However, this is due to stringing, a typical production problem in the FFF 3D printing process caused by excess filament oozing out of the nozzle during travel moves. This can also be observed in the original file (Figure 5.4(a)). While elevations were well reconstructed, the method struggled to capture depressions in the geometry. Thus, the writing on the geometry's outer side was hardly captured.

(a)   (b)
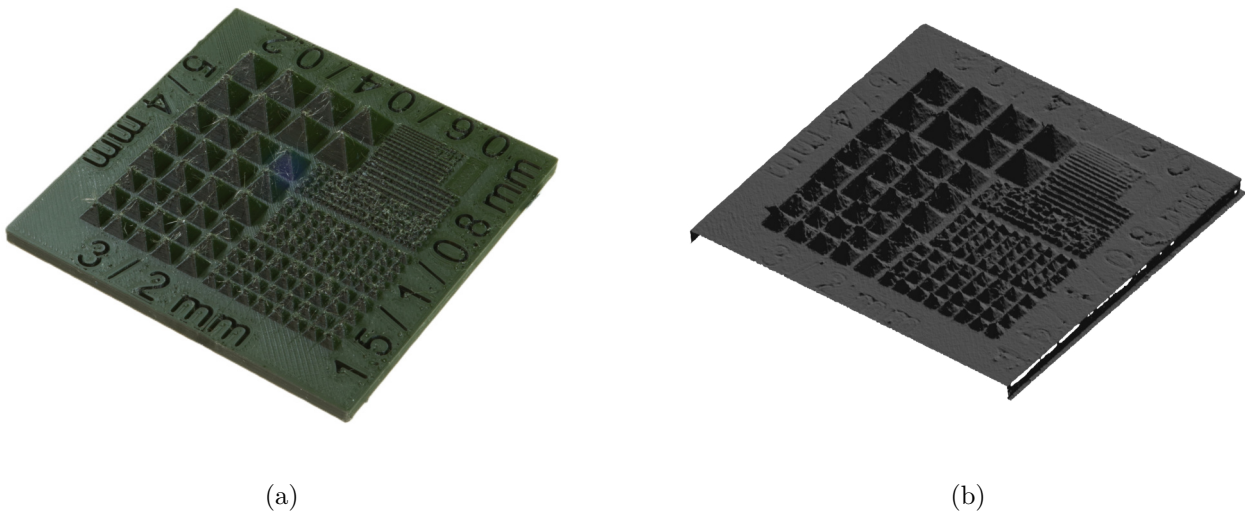
Figure 5.4: (a) Sample geometry and (b) photogrammetric reconstruction.

Accuracy Measurement based on a Known Geometry

To evaluate the method's accuracy, a 3D-printed ice-accreted profile was digitized, and the resulting digital copy was compared with the STL file of the reference geometry. Figure 5.5(a) shows the deviation as calculated Hausdorff distance between the copy and the reference file as a three-dimensional contour plot and the corresponding histogram. Figure 5.5(b) shows the approximated graph of the beta PDF and visualizes the calculated expected value, mean value, and median.

<div align="center">(a)   (b)</div>
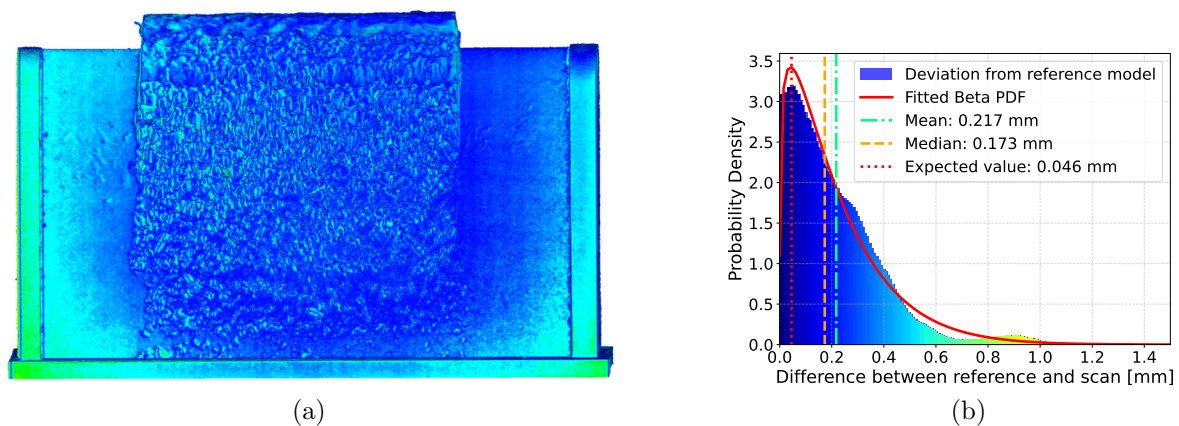
Figure 5.5: Deviation between reference geometry and its copy is shown as (a) a three-dimensional contour plot and (b) a histogram with an approximated function of the beta distribution.

Except for a few outliers, the deviations range to around 1 mm, with an average deviation of 0.217 mm and a median of 0.173 mm. As these parameters are susceptible to outliers, the expected value determined by the beta PDF is significantly lower at just 0.046 mm. Also worth mentioning is the fact that the deviations are smaller in the center of the object on which the camera was focused than at the edges. Therefore, correct focusing also seems to have a positive effect on quality.

Repeatability of the Object's Pose

The repeatability of the referencing was investigated by creating three independent datasets from a propeller blade and calculating the individual distances to the reference CAD file. The rotation angles and distances for the reference alignment were determined manually in the CAD program for Dataset 1, and the transformed coordinates were assigned to the individual models so that they all had the exact marker coordinates. The calculated Hausdorff distances to the reference CAD file are shown in Figure 5.6 as a histogram and 3D contour plot. In addition, the green histogram shows the differences between the calculated deviation of the individual bins for Datasets 2 and 3 to Dataset 1, which was used for reference alignment. Dataset 1 shows a similar course of the deviations as in Figure 5.5 for the previously performed accuracy measurement. This error can, therefore, be attributed to the accuracy of the photogrammetry or the manual determination of the transformation parameters. Datasets 2 and 3 show slightly more significant deviations. This difference can be attributed to an error in the referencing. For Dataset 2, this mean error of the absolute differences is 0.190 mm; for Dataset 3, it is 0.117 mm. The mean deviations from the reference file and the means of the absolute differences of the deviations to Dataset 1 are listed in Table 5.1.

(a)   (b)   (c)
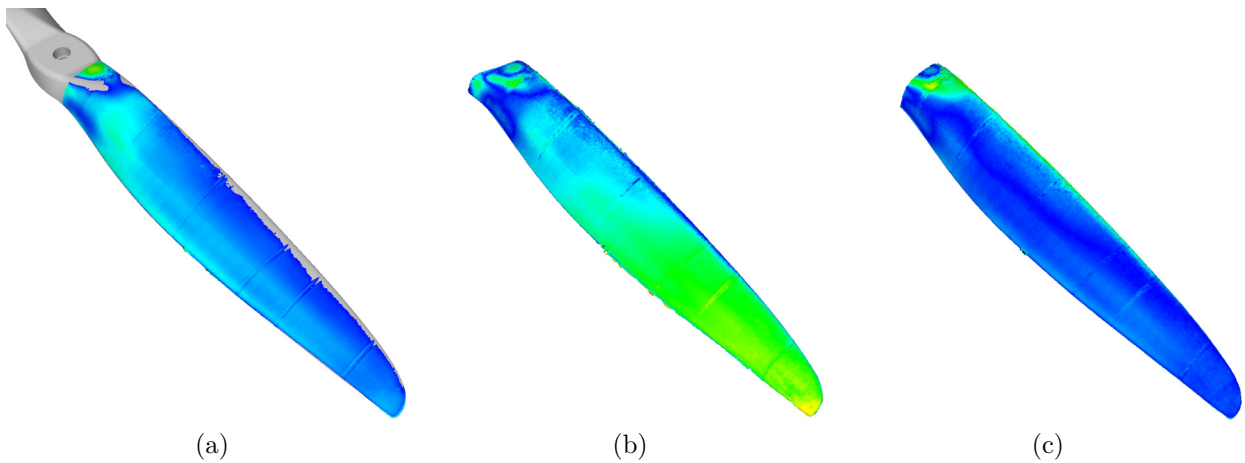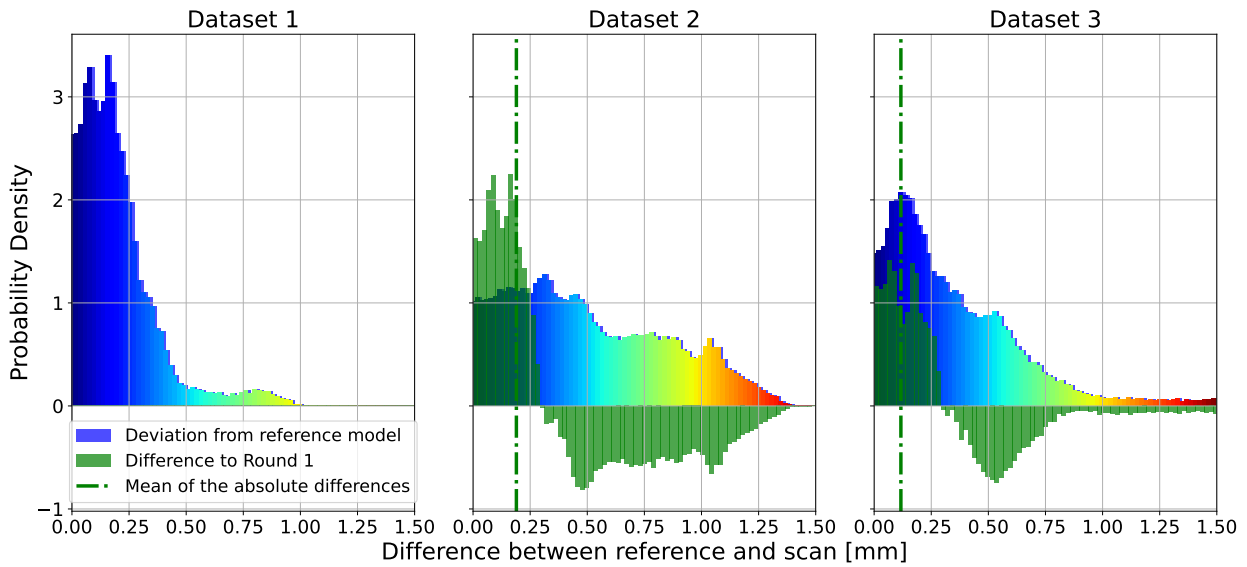
Figure 5.6: Deviations between three individual datasets captured of a propeller blade and its
CAD geometry. In addition, the green histogram shows the differences between
the calculated deviation of the individual bins for Datasets 2 and 3 to Dataset
1, which was used for reference alignment.

Table 5.1: Mean deviations from reference file and means of the absolute differences of the
deviations to Dataset 1.

	Dataset 1	Dataset 2	Dataset 3
Mean deviation from reference file [mm]	0.207	0.514	0.423
Mean of the absolute differences of the deviations to Dataset 1 [mm]	-	0.190	0.117

5.3 Further Method Refinement

This section presents the results of all further tests carried out to gain knowledge for potential optimization of the method.

Optimization of the Camera Parameters

Several series of images were taken with different settings for aperture, ISO sensitivity, and shutter speed to find the ideal camera parameters for capturing ice features. Tests were divided into two parts to examine the parameters independently and carried out on non-iced airfoils and with accreted airfoils of various types of ice. First, the airfoil was photographed with varying sizes of aperture and ISO values at equivalent exposure; then, in the second test, the ISO and aperture were kept constant (ISO 100 and $f/13$), and the exposure increased gradually. The result was quantified and compared using the common features found in the images, known as tie points.

Figure 5.7 shows the number of tie points found in the images for the first test series of a non-iced airfoil. It can be seen that lower ISO values cause more tie points. The highest number of tie points gained for all ISO values is at a f-stop setting for the aperture of $f/13$. By drifting away from this optimum, the number of tie points reduces.
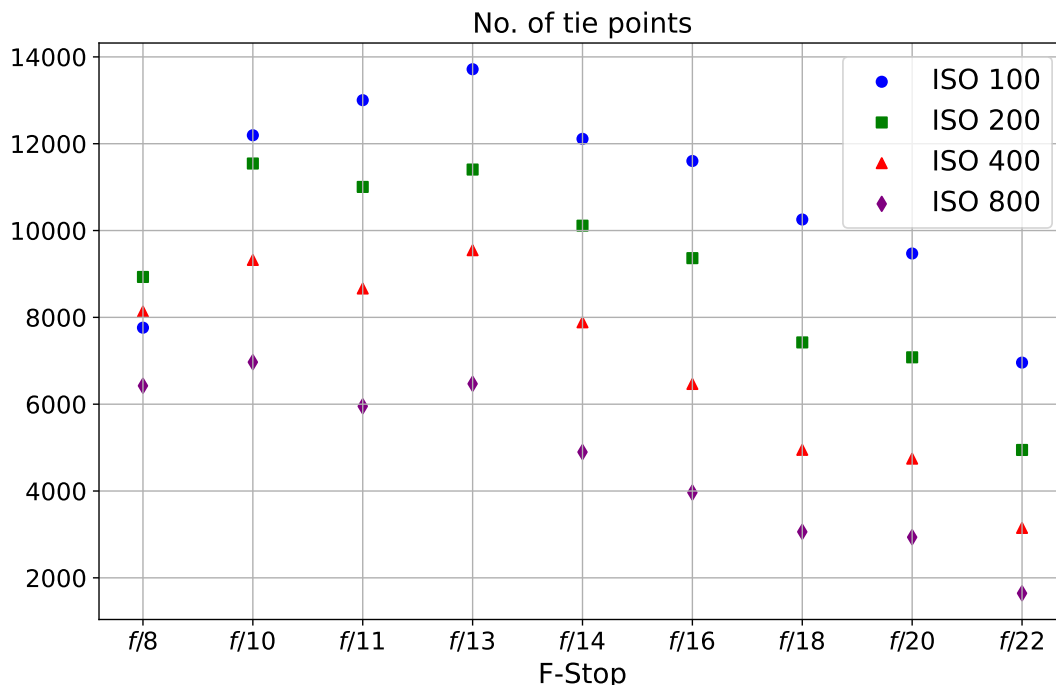
Figure 5.7: Number of tie points found depending on the ISO sensitivity and aperture of the images for a non-iced airfoil.

The same test was later performed with iced airfoils for rime, glaze, and mixed ice (Figure 5.8). Here, as well as the clean airfoil, the lower ISO sensitivity shows the best results. However, the optimum aperture size shifts to a slightly higher f-stop of $f/16$. Also noticeable is the drop in tie points with mixed ice at an aperture setting of $f/11$, which is replicated at both ISO values. It is uncertain where this drop comes from, but a measurement error can be assumed since it is not repeated in the other cases. The total number of tie points for the ice-accreted airfoils is higher than for the non-iced airfoils, which is probably due to the fact that the ice has more contours and edges than the clean airfoil.
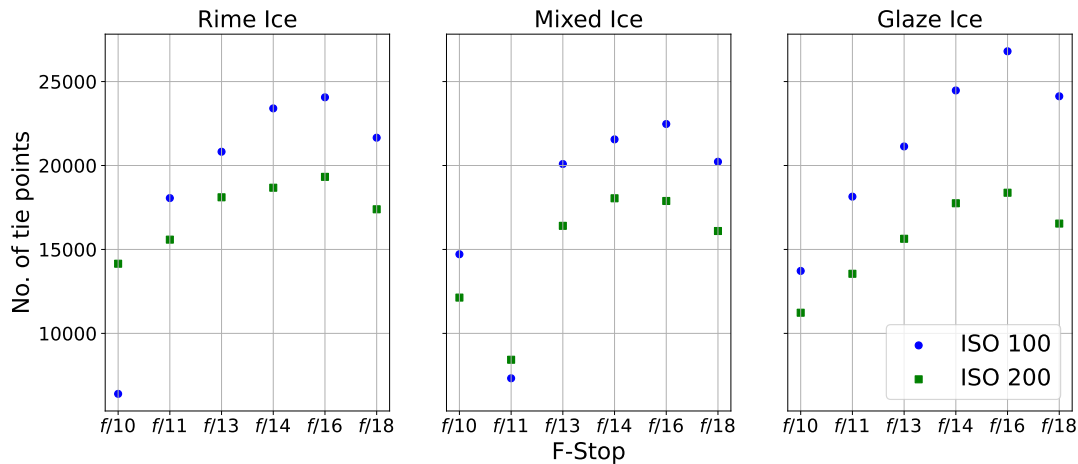
Figure 5.8: Number of tie points found depending on the ISO sensitivity and aperture of the images for different ice types.

Figure 5.9 shows the resulting tie points for the different exposure times. There is no discernible trend in the results here. Only images that are too dark, taken with a shutter speed of less than 1/6 sec, show an apparent decrease in the number of tie points for the ice-accreted airfoils. However, when evaluating the results, it must be considered that too high exposure can also worsen the result without the number of tie points decreasing noticeably. Figure 5.10 shows the tie points found by Metashape (blue dots) in the same image, taken with different shutter speeds. Due to its white color, the ice loses contrast to its surroundings with increasing exposure. Accordingly, there are hardly any tie points on the ice accretion (upper part) in the right image with high exposure time. On the other hand, the dark airfoil (lower part) still shows a high contrast to its surroundings so that the algorithm can find many feature points. In the case of glaze ice, a too-high exposure time also results in a drop of tie points.
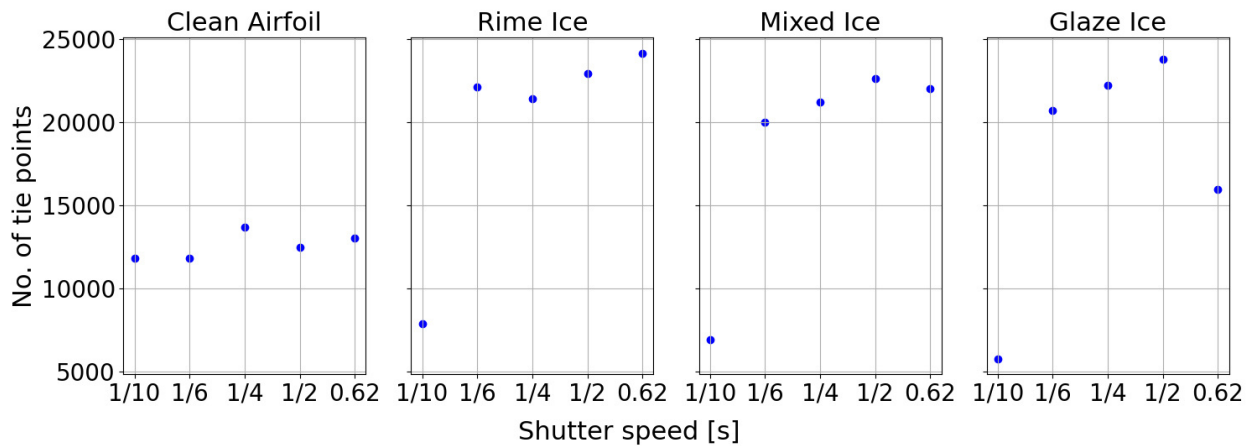
Figure 5.9: Number of tie points found depending on exposure of the images for different ice types.
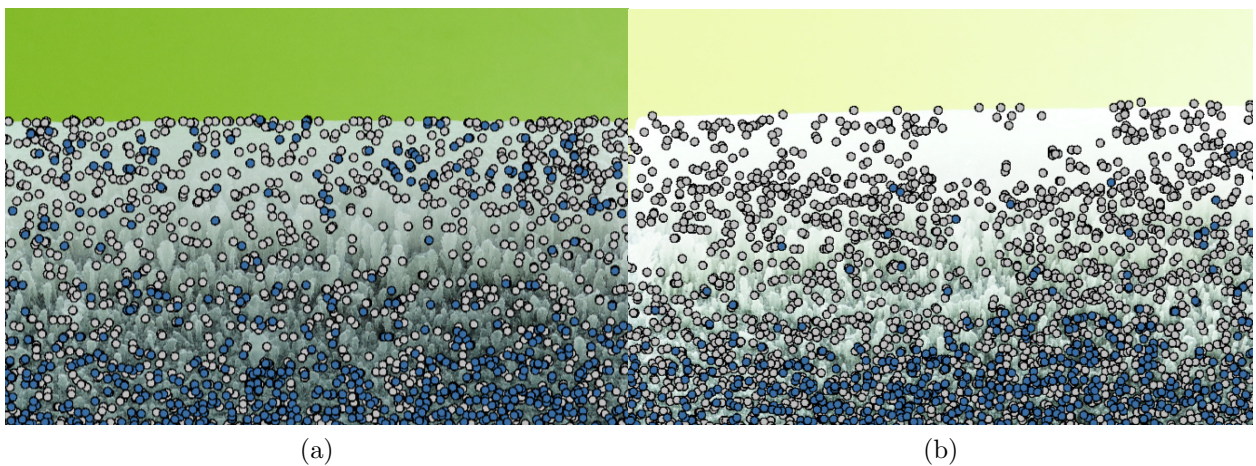
Figure 5.10: Detected key points (gray) and tie points (blue) in the same image taken with shutter speeds set to (a) 1/6 sec and (b) 0.6 sec. At high exposure, ice loses contrast to its surroundings and fewer tie points are detected.

Image Acquisition: Smartphone vs. Professional Camera

For the comparison of smartphone and professional cameras, the same geometry was used as in the section "Minimal Resolvable Feature Size" . The specimen was reconstructed using photogrammetry based on images taken with the Apple iPhone SE (2nd generation) and the Sony ILCE-6400. The results, shown in Figure 5.11 and Table 5.2, were compared to examine whether a smartphone camera could replace a professional camera in the image acquisition process. On the left is the original geometry; in the middle is the reconstructed 3D model based on images from the professional camera; and on the right is the model based on photos made with the smartphone. The smartphone delivered significantly poorer results

here. Compared to the results from the Sony camera, the surface is much less smooth, and the individual pyramids merge into each other. This is also reflected in the number of tie points, which is more than 2.5 times higher for the professional than for the smartphone. The same applies to the number of computed depth maps and dense cloud points, which is almost three times higher.

<div align="center">(a)   (b)   (c)</div>
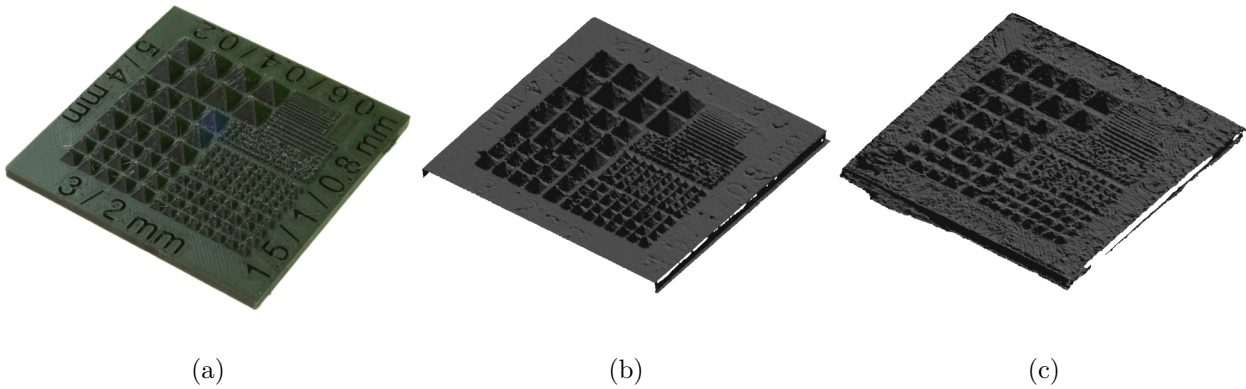
Figure 5.11: (a) Sample geometry, (b) reconstructed based on photos made with a Sony ILCE-6400 camera and (c) with the smartphone Apple iPhone SE (2nd generation).

Table 5.2: Professional camera vs. smartphone camera: SfM parameters.

	Sony ILCE-6400	Apple iPhone SE
Tie points	280,984	105,676
Tie points (after optimization)	57,434	20,549
Depth Maps	209	139
Dense Cloud points (confidence > 10%)	2,600,952	882,171

Number of Cross Sections for Representative MCCS

This study aimed to determine the number of section cuts required to obtain a representative cross-sectional area of the resulting MCCS. For this purpose, the number of section cuts at different spans was iteratively increased, and the cross-sectional area of the MCCS was plotted. The result for the three different ice types is shown in Figure 5.12. First, it is noticeable that the area of the MCCS increases with the number of section cuts as more three-dimensional features are projected into the plane of the MCCS. Larger spans also result in a larger cross-sectional area. The results between the spans drift significantly further apart at warmer temperatures (glaze ice) than at colder temperatures (rime

ice). This indicates that these have more 3D features and, thus, a more inhomogeneous distribution of ice accretion in the span direction. The gradient decreases as the number of cross-sections increases but does not converge for any ice types within the tested range of a maximum of 50 section cuts.
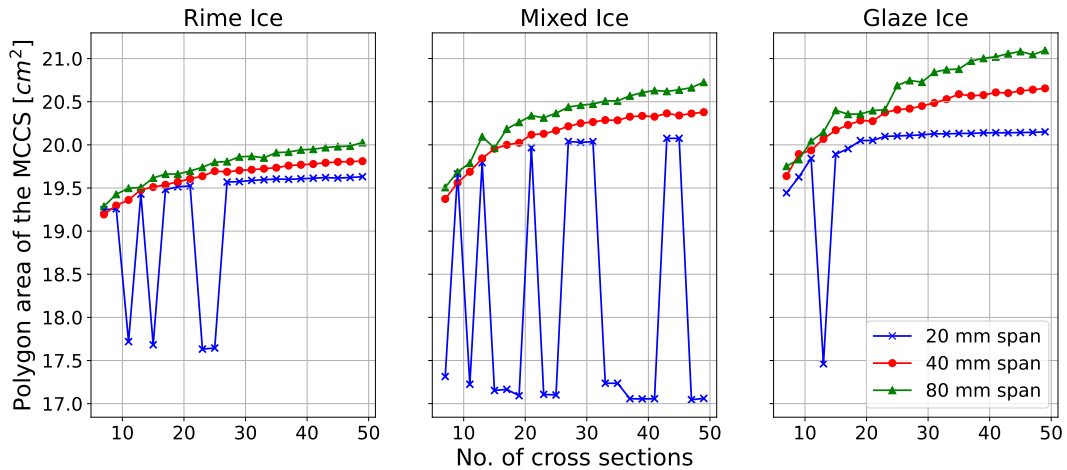
Figure 5.12: Area of the envelope of the MCCS for different spans with increasing number of section cuts.

These results also noticeably show significant drops in the cross-sectional area at spans of 20 mm. This phenomenon particularly affects the mixed ice case. This can be traced back to an error in generating the alpha-shaped envelopes. The alpha shape function attempts to create a boundary that encloses the set of points. However, it may result in the calculation of an envelope that encloses the points from the inside instead of the outside, as shown in Figure 5.13. Larger spans do not appear to be affected by this.
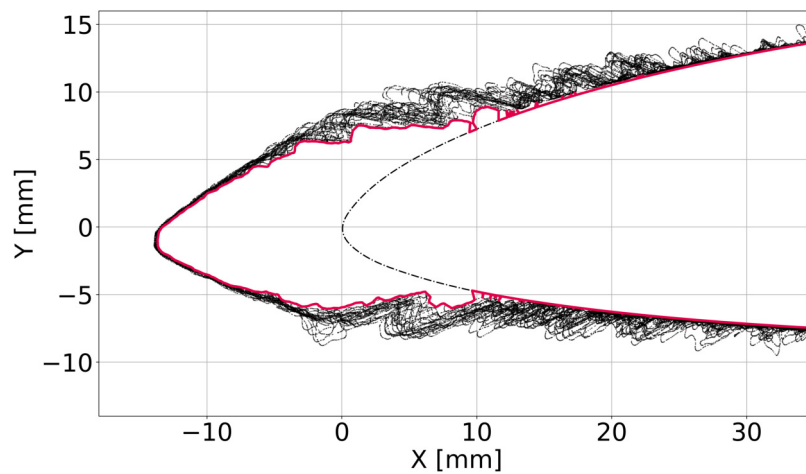
Figure 5.13: Incorrect calculation of the MCCS.

Number of Cross Sections for Representative Ice Volume and Density

Similar to the convergence study of the cross-sectional area from the MCCS, it was investigated how the number of section cuts affects the numerically approximated ice volume and, thus, the ice density. For this purpose, the volume was plotted as a function of the number of cross-sections. The ice accretion was trimmed to around 100 mm in legth to have the same reference for all test series. The results are shown in Figure 5.14. The measured difference between the mass of the airfoil with and without ice accretion was divided by the calculated volume to determine the ice density (red line with data points). The average of the last ten values was defined as convergence value (blue dash-dot line) to calculate a "final" value for the volume and density. The number of section cuts was then determined for which the volume deviated from the convergence value by a maximum of 1 % for the first time (blue dashed line). Rime and mixed ice reach the defined criterion at around 25 section cuts. Glaze ice reached it earlier at around 15 section cuts. Contrary to the other two cases, rime ice does not converge within the examined range of 41 section cuts. The calculated ice volume and density are listed in Table 5.3. The literature values listed for comparison originate from a study published by the National Aeronautics and Space Administration (NASA), in which density measurements for the various ice types were carried out in an IWT [54]. While the calculated value for the density of glaze ice agrees well with the value from the study, the values for rime and mixed ice differ significantly. Since rime ice essentially contains air and forms ice feathers, the lower value is nevertheless plausible. However, the calculated density of mixed ice is too high. This may be the result of a statistical error e.g. incorrect weighing.
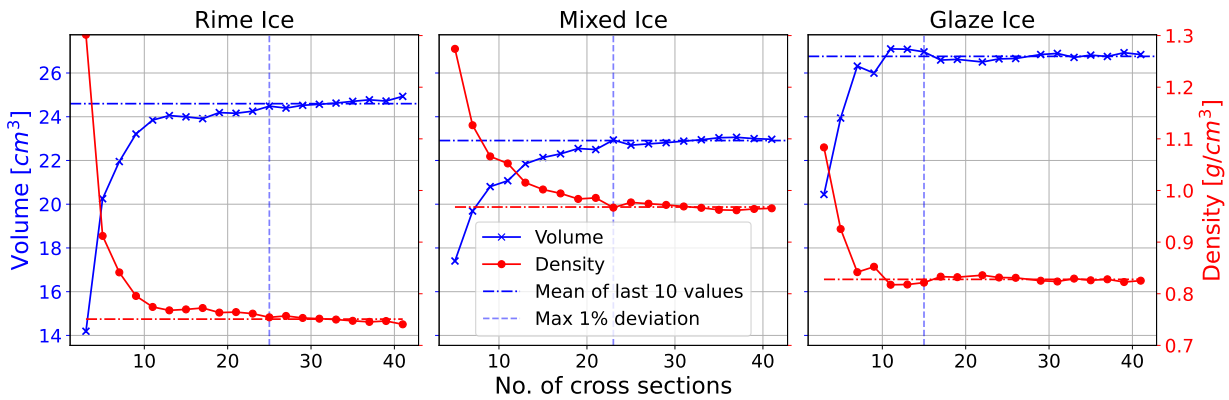
Figure 5.14: Calculated ice volumes and densities with increasing number of section cuts.

Table 5.3: Calculated volumes and densities for various ice types.

	Rime Ice	Mixed Ice	Glaze Ice
Volume [cm^3] (Ice accretion trimmed to 100 mm)	24.598	22.911	26.761
Measured mass [g]	18.469	22.176	22.154
Density calculated [g cm^{-3}]	0.751	0.968	0.828
Density from literature [g cm^{-3}] [54]	0.873	0.885	0.875

6 Discussion

In this chapter, the obtained results will be discussed and placed in the context of the knowledge gained in this thesis. The sequence of the previous chapters will be followed again, starting with the overall validation of the developed method, then the accuracy assessment, and, further method refinements. Finally, the SfM approach will be compared qualitatively with other techniques for digitizing ice.

6.1 Validation

The developed and optimized method was tested and validated in practice during an IWT test campaign at the VTT in Helsinki. All ice shapes and types, rime, glaze, and mixed ice, could be reconstructed with good quality and a high level of detail (Figure 5.1). Even small details, such as ice feathers on rime ice, are clearly visible. Due to ice shedding, the ice shapes on the propeller blades are much more delicate but could also be captured in good quality. Due to technical problems with the propeller test rig, it was not possible to test glaze and mixed ice on the propeller blades. However, based on the results on the airfoil and the rime ice case on the propeller blades, it can be assumed that these could have been reconstructed to a similar quality.

The automated scaling and referencing of the digitized models is a significant improvement over the previous state of research at the UAV Icing Lab. The scaling was achieved with high precision and repeatability. Referencing and alignment also worked reasonably well, particularly for the airfoil (Figure 5.2). A single test run showed a slight angular offset, leading to a few millimeter deviations. It is possible that the airfoil may not have been inserted correctly into the base plate. To prevent this, the grooves of the base plate into which the test specimen is inserted could be made slightly conical. This design measure would allow the airfoil to self-center and thus enable a more reproducible alignment with respect to the markers. The two grooves of the same length, which previously had the same length and width, could also be designed with different dimensions to prevent the airfoil from being placed "the wrong way round" on the base plate, thus changing the pose to the markers. Coincidentally, this never happened during the tests. Nevertheless, this measure would eliminate another potential source of error.

The propellers showed a slight lack of precision, particularly at the blade tip, which indicates a slight angular misalignment around the x-axis (Figure 5.3). Since the propellers are fixed by screwing them to the frame, the divergences between the individual runs are probably not due to a mechanical cause but to the SfM reconstruction process or the inaccurate

referencing. The manual measurement of the marker coordinates, in particular, leaves room for improvement. However, this error can hardly be avoided due to the length of the propeller blade. In the case of the investigated 21" propeller (which has a radius of 266.7 mm), a slight offset angle of 0.2 - 0.4 ° is already sufficient to cause the observed 1 - 2 mm error at the blade's tip.

Another possible source of error is the painting of the ice shapes. This was done manually and is, therefore, not repeatable. Due to the sometimes complex geometric structures, ensuring that everything was painted evenly is also impossible. Drying the paint in the freezer could also slightly affect the results. However, due to the low layer density of the airbrush application, this error is unlikely to affect the ice geometry itself, but it affects its roughness. Ice roughness was not investigated further in this thesis, but it could be important in future work.

Further significant improvements compared to the previous state of research are automating the photogrammetry process in Metashape through scripting and image acquisition with the camera mount designed for this purpose. Both measures enable significantly faster and more reproducible results and simplify the process. Based on the results in the IWT, the method could be validated successfully overall.

6.2 Accuracy Assessment

The second aim of this work was to investigate the method's accuracy. Various tests were carried out for this purpose. The investigation of the minimal resolvable feature sizes has shown that even small features of 0.4 mm are detected and reconstructed (Figure 5.4). More minor features can no longer be identified in the reconstruction, but the 3D printing process used to produce the test specimen also reaches its limits here. However, it should be mentioned that the features to be examined are elevations in the geometry, which seem to be much easier to digitize than depressions. For example, the engraved writing into the test object was not captured despite its larger dimensions.

Nevertheless, the accuracy measurement based on a known geometry showed that features with a shape similar to the ice accretion could be captured very accurately (Figure 5.5). The mean deviation from the reference object is 0.217 mm, and the median is 0.173 mm. As both values are sensitive to outliers, the expected value approximated via the beta PDF is significantly lower at just 0.046 mm. Nevertheless, there appear to be some individual outliers that exceed 1 mm. It is uncertain where these outliers come from; they may be due to pixel errors, image grain, or an error in calculating the Hausdorff distance in MeshLab. Due to their small number, however, the model itself is practically unaffected. With deviations far below one millimeter, SfM photogrammetry can be rated as reasonably accurate overall.

As the IWT results showed slight offsets between the runs, the repeatability of the referencing was additionally examined. The first reconstruction, aligned with the reference file, showed a similar histogram curve and mean value as the previous test, analyzing the photogrammetry's accuracy and thus confirming its validity (Figure 5.6 and Table 5.1). The two further reconstructions, referenced according to the aligned and transformed coordinates, showed significantly higher deviations compared to the first dataset. Assuming that the error in the mechanical fastening of the propeller blade is negligible, this error can be deduced from the referencing error. In the deviation histogram, these errors range to over 1.5 mm, roughly corresponding to the offset at the propeller tip from the IWT tests. However, the counts in these areas are relatively low and show an average offset of 0.190 mm (Dataset 2) and 0.117 mm (Dataset 3) to the first reconstruction. This is well below the observed results from the IWT. It cannot be conclusively clarified why the alignment from the IWT tests is less precise. Still, it should be noted that the accuracy tests were carried out under laboratory conditions. In the IWT, conversely, vibration can affect the results, and the permanent cold and duration of the tests increase the chance of human error.

6.3 Further Method Refinement

This section discusses the results of further tests to improve the process of digitizing ice shapes and gain a better understanding. The focus will first be on the image acquisition process, followed by the application of the post-processing and the number of 2D section cuts needed to represent the 3D ice shape.

Image Acquisition and Optimal Camera Parameters

The basis of SfM photogrammetry is always the captured images of the object of interest. Therefore, the quality of the images as input data is critical for good output quality. The investigations have shown that selecting the correct camera settings is essential. Specifically, this means that ISO sensitivity, aperture size, and shutter speed should be adjusted manually. Smaller ISO values caused more tie points to be detected in the software, thus better alignment (Figure 5.7 and 5.8). This is probably due to grain in the photos, which is caused by higher ISO sensitivity, making alignment more difficult. Furthermore, there is a trend towards an optimal aperture size between $f/13$ and $f/16$, whereby the optimal f-stop value is somewhat higher for ice. It is uncertain where this difference comes from; it is probably based on the optical properties of the ice. Therefore, a good range between $f/13$ and $f/16$ can be assumed for aperture rather than a universally applicable ideal value. Smaller f-stop settings reduce the image's depth of field and, thus, the extent to which features are clearly depicted. F-stop settings higher than $f/16$ probably cause diffraction effects due to the small aperture, which can harm the image quality. Both effects can be seen in the decreasing number of tie points when increasing the distance from the aperture optimum. The exposure should be long enough so that features are well-exposed and can be recognized by the SfM software. However, exposure times that are too high have shown that details in the ice can be lost despite the same or even increasing number of tie points

found in the images (Figure 5.9 and 5.10). The optical properties of the ice and the airfoil can explain this phenomenon. While the ice quickly loses its contrast to its surroundings due to its white color, the software still recognizes numerous features and details in the black airfoil. As a rule of thumb based on experience, the tone values in the histogram should be around the upper third of the luminance scale. The exposure is also determined by the ISO value and the aperture size, so it is advisable to set these first and then adjust the shutter speed.

Using a standard smartphone instead of a professional camera to simplify image capture did not prove to be a promising alternative. The results of the SfM reconstruction based on the images taken with the smartphone were significantly worse compared to the professional camera (Figure 5.11 and Table 5.2). This could be explained by the fact that the smartphone has more limited hardware and instead corrects images using software that "beautifies" the photos for the user. For example, the smartphone has a non-adjustable aperture with a relatively large aperture size of $f/1.8$. Although this allows a large amount of light to enter the camera, the depth of field is drastically reduced, and the outer areas of the image are approximated instead. In everyday use, for which the smartphone is designed, this is mostly not noticeable. However, in photogrammetry, where the output quality is based on the input quality of the images, the smartphone has a clear disadvantage compared to the professional camera. It is possible that the results were better with later smartphone models, some of which have more advanced dual-camera systems. However, due to the advanced algorithms used to pre-process the images, it is difficult to understand the image-capturing process and make specific adjustments. The approach of using a smartphone rather than a professional camera could be used for a very quick and cheap assessment in the field; however, for good output quality, the professional camera should be used.

Number of Cross Sections for 3D Evaluation

It was shown that the MCCS application and the determination of ice volume and density depend significantly on the number of section cuts over which they are determined. The cross-sectional area of the MCCS increases with the number of section cuts (Figure 5.12). The gradient becomes smaller but does not converge. However, the change is relatively small, especially for small spans. A reasonably accurate representation of the MCCS can be assumed for about 30 sections without having to deal with excessive calculation times. For larger spans, especially for glaze ice, the number of section cuts should be adjusted to capture 3D features sufficiently accurately. For small spans (20 mm), the algorithm often applied the envelope incorrectly by creating the hull inside the point cloud instead of from the outside (Figure 5.13). It is unknown where this phenomenon originates, but it did not appear at larger spans.

The approximated volume based on the number of section cuts shows a similar but more distinct curve (Figure 5.14). For glaze ice, the volume converges at around 15 section cuts and mixed ice at around 23 cuts. For rime ice, the volume does not converge, but the change

is relatively small at about 25 and more section cuts. The ice density calculated from the volume for glaze ice is 0.828 $\mathrm{g\,cm^{-3}}$, therefore relatively close to the value from literature published by NASA (Table 5.3). The calculated density of 0.751 $\mathrm{g\,cm^{-3}}$ for rime ice is also plausible. Although the value is below the literature value, the density of rime ice will likely fluctuate significantly due to the air inclusions. These results validate the designed approach for calculating the ice volume and, thus also, the accuracy of the photogrammetric approach to digitize ice shapes. Only the density calculated for mixed ice is significantly too high. However, this might be a statistical error which could be investigated by evaluating more samples.

6.4 Comparison with other Ice Measurement Methods

Compared to other optical methods, such as laser scanning, the most significant advantage of SfM photogrammetry is the low cost of hardware. Camera, lens, turntable, photo studio, etc., cost hardly more than $ 1500 [39, 40, 41, 42]. The 3D reconstruction software Metashape is more expensive, at around $ 3500 in the Professional Edition [55], but still far below the costs of standard 3D scanners, which can easily be in the five-figure range. In addition, the simple setup enables a quick installation and, thus, flexible application options regarding location. With an average absolute deviation of around 0.22 mm, the accuracy of SfM photogrammetry is also at a high level, comparable to that of other established methods. Gong and Bansmer claim a measurement uncertainty of 0.15 mm for their laser scanning method [28]. For Liu's approach with structured light, the reconstruction error is "less than 0.5 mm" [33]. The mold-and-cast technique is probably mainly limited by the handling of the molds and shrinkage effects, which are assumed to be around 0.1 mm [32]. However, the accuracy comparison should be treated with caution, as reconstruction errors and accuracy values were determined differently, and human errors due to incorrect handling often predominate. The comparative use of different techniques under the same conditions could be investigated in future studies.

A disadvantage is that SfM photogrammetry in this setup only allows stationary measurements, meaning that ice growth cannot be measured. The computational effort is also significantly higher than that of 3D scanners, which makes real-time evaluation impossible. In addition, SfM requires a certain degree of expertise and experience in photography and the operation of Metashape compared to commercially available 3D scanning systems. However, the process has been designed as straightforwardly as possible, and the necessary know-how can be quickly learned. Overall, it can concluded that, despite these challenges, photogrammetry's ability to capture detailed three-dimensional geometry and its low cost make it a suitable and cost-efficient tool for digitizing ice shapes.

7 Conclusion

The first goal of this work was to develop an SfM photogrammetry process for digitizing ice shapes from experimental tests in the IWT. Digitizing ice shapes allows for quantifying the extent and distribution of ice accretion on the surfaces of UAV components. This will also enable subsequent evaluation and validation of the simulation models designed by the UAV Icing Lab. Based on methods already used sporadically, the process was to be adapted and optimized to make it as simple, standardized, and repeatable as possible, thus practical for experimental research.

The results of the IWT test campaign show that this goal was achieved highly successfully. The ice shapes created there were all captured and digitized with a high level of detail and precision. A significant improvement on the previous state of research at the UAV Icing Lab is the automated scaling and referencing of the reconstructed models using GCPs. This method also proved to be successful. A reasonably accurate and precise alignment to the reference geometry was achieved with a deviation of only a few tenths of a degree or millimeters. Other notable improvements in the photogrammetry process are the automation of the SfM reconstruction in Metashape through scripts and the significantly simplified and more reproducible image acquisition through a camera frame. The quick-release system allows to quickly change the camera to different positions. All these measures make the photogrammetry process faster, simpler, and more standardized.

The second objective was to investigate the accuracy of the applied method. Various tests were carried out for this purpose and compared with known geometries. Under laboratory conditions, both the reconstruction error and alignment errors are well below one millimeter. SfM photogrammetry is also capable of recognizing and reconstructing small features and details with sizes down to a few tenths of a millimeter. Overall, the accuracy can be rated relatively high and sufficient for the practical application of ice-shape digitization.

In addition, post-processing methods were further developed and investigated, in particular for the two-dimensional representation of three-dimensional features. It was shown that the ice volume can be determined reasonably accurately with a simple approximation approach. These results were validated with the calculated ice densities, which were compared with literature values. The concept of the MCCS and the influence of the number of section cuts and spacing between them on the cross-sectional area were also investigated.

The extent to which settings for the MCCS and other post-processing methods are representative of the validation of ice accretion simulation models must be investigated in

future CFD studies. In addition, the digital ice shapes can be used to test aerodynamic performance degradation in a conventional wind tunnel. Based on the reconstructed data, artificial ice shapes can be produced and examined, e.g. by rapid prototyping. This also allows simulated results from performance degradation models to be validated and adjusted if necessary. For the investigation of aerodynamic degradation, the roughness of the ice must be taken into account, which was not investigated further in this study. However, it can be significantly influenced by the coloring of the ice shapes. Furthermore, performing the accuracy tests under field conditions in the IWT might make sense to check whether the environment affects the results.

In conclusion, photogrammetry has proven to be an effective and cost-efficient tool for digitizing ice shapes. Compared to other 3D scanning methods, the costs for hardware and software are fairly manageable, making it an economically viable option for research. Nevertheless, it has been shown that photogrammetry is capable of capturing even small details and reconstructing them with sufficient precision and accuracy. Compared to commercially available 3D scanning systems, the application requires slightly more extensive knowledge and experience in image acquisition and 3D reconstruction. However, the process has been designed as straightforwardly as possible, and the necessary know-how can be quickly learned.

Bibliography

[1] SHAKHATREH, H. ; SAWALMEH, A. ; AL-FUQAHA, A. ; DOU, Z. ; ALMAITA, E. ;
    KHALIL, I. ; OTHMAN, N. S. ; KHREISHAH, A. ; GUIZANI, M.: *Unmanned Aerial
    Vehicles: A Survey on Civil Applications and Key Research Challenges.* In: *SAE Inter-
    national* (2018)

[2] INTERNATIONAL CIVIL AVIATION ORGANIZATION: *Global Air Traffic Management
    Operational Concept (Doc 9854).* 2005. – URL: https://www.icao.int/Meetings/
    anconf12/Document%20Archive/9854_cons_en%5B1%5D.pdf. – Access date: 2023-10-
    23

[3] SØRENSEN, K. L. ; BORUP, K. T. ; HANN, R. ; BERNSTEIN, B. C. ; HANSBØ M.:
    UAV Atmospheric Icing Limitations: Climate Report for Norway and surrounding. In:
    UBIQ Aerospace (2021). – URL: https://www.ubiqaerospace.com/climate-report.
    – Access date: 2023-10-23

[4] HANN, R.: *Atmospheric Ice Accretions, Aerodynamic Icing Penalties, and Ice Pro-
    tection Systems on Unmanned Aerial Vehicles.* Trondheim, Norwegian University of
    Science and Technology, PhD thesis, 2020

[5] BRAGG, M. B. ; BROEREN, A. P. ; BLUMENTHAL, L. A.: *Iced-airfoil aerodynamics.* In:
    Elsevier Ltd. 41 (2005), No. 5, S. 323–362

[6] WESTOBY, M. J. ; BRASINGTON, J. ; GLASSER, N. F. ; HAMBREY, M. J. ; REYNOLDS,
    J. M.: *'Structure-from-Motion' photogrammetry: A low-cost, effective tool for geoscience
    applications.* In: *Geomorphology* 179 (2012), S. 300–314. – ISSN 0169555X

[7] TICE, B. P.: *Unmanned Aerial Vehicles: The Force Multiplier of the
    1990s.* 1991. – URL: https://web.archive.org/web/20090724015052/http://www.
    airpower.maxwell.af.mil/airchronicles/apj/apj91/spr91/4spr91.htm. – Access
    date: 2023-10-23

[8] BERGEN, P. ; SALYK-VIRK, M. ; STERMAN, D.: *World of Drones.* 2020-07-30. – URL:
    https://www.newamerica.org/future-security/reports/world-drones/. – Access
    date: 2024-04-24

[9] HANN, R. ; JOHANSEN, T. A.: *Unsettled Topics in Unmanned Aerial Vehicle Icing.* In:
    SAE International (2020)

[10] CAO, Y. ; TAN, W. ; WU, Z.: *Aerospace Science and Technology.* Bd. 75: *Aircraft
    icing: An ongoing threat to aviation safety.* Elsevier, 2018

[11] BERNSTEIN, B. C. ; WOLFF, C. A. ; MCDONOUGH, F.: *An Inferred Climatology of Icing Conditions Aloft, Including Supercooled Large Drops. Part I: Canada and the Continental United States.* In: *Journal of Applied Meteorology and Climatology* 46 (2007), No. 11, S. 1857–1878. – ISSN 1558-8424

[12] GENT, R. W. ; DART, N. P. ; CANSDALE, J. T.: *Aircraft icing.* In: *Philosophical Transactions of the Royal Society of London. Series A: Mathematical, Physical and Engineering Sciences* 358 (2000), No. 1776, S. 2873–2911. – ISSN 1364-503X

[13] BERNSTEIN, B. C. ; RATVASKY, T. P. ; MILLER, D. R. ; MCDONOUGH, F.: *Freezing Rain as an In-Flight Icing Hazard.* In: *Conference on Aviation, Range and Aerospace Meteorology* 8 (2000). – URL: `https://ntrs.nasa.gov/api/citations/20000063509/downloads/20000063509.pdf`. – Access date: 2023-10-25

[14] LINDNER, M. ; WALLISCH, J. ; HANN, R.: *UAV Icing: Numerical Simulation of Icing Effects on Wing and Empennage.* In: *SAE International Conference on Icing of Aircraft, Engines, and Structures.* (2023)

[15] KRAUS, K.: *De-Gruyter-Studium.* Bd. Bd. 1: *Photogrammetrie: Geometrische Informationen aus Photographien und Laserscanneraufnahmen.* 7., vollst. bearb. und erw. Aufl. Berlin : de Gruyter, 2004. – ISBN 3-11-017708-0

[16] HATAJI, Y. ; KUROSHIMA, H. ; FUJITA, K.: *Motion parallax via head movements modulates visuo-motor control in pigeons.* In: *The Journal of experimental biology* 224 (2021), No. Pt 3

[17] BETLEM, P. ; RODES N. AND CONTRIBUTORS: *Geo-SfM course from the University of Svalbard: Session 1: Metashape Tutorial & Session 4: Small object SfM photogrammetry.* 2024. – URL: `https://unisvalbard.github.io/Geo-SfM/landing-page.html`. – Access date: 2024-02-14

[18] LOWE, D. G.: Object recognition from local scale-invariant features. In: *Proceedings of the Seventh IEEE International Conference on Computer Vision*, IEEE, 1999, S. 1150–1157 vol.2. – ISBN 0-7695-0164-8

[19] FURUKAWA, Y. ; HERNÁNDEZ, C.: *Foundation and trends in computer graphics and vision.* Bd. 9,1/2: *Multi-view stereo: A tutorial.* Boston and Delft : Now, 2015

[20] MA, Y. ; SOATTO, S. ; KOŠECKÁ, J. ; SASTRY, S. S.: *Interdisciplinary applied mathematics Imaging, vision, and graphics.* Bd. 26: *An invitation to 3-D vision: From images to geometric models.* New York and Berlin and Heidelberg : Springer, 2004. – ISBN 978-1-4419-1846-8

[21] VAN RIEL, S.: *Exploring the use of 3D GIS as an analytical tool in archaeological excavation practice*, Lund University, Master's thesis, 2016. – URL: `https://www.researchgate.net/figure/`

Structure-from-Motion-SfM-photogrammetric-principle-Source-Theia-sfmorg-2016_
fig3_303824023. – Access date: 2023-11-08

[22] CUCCI, D. A.: *Accurate optical target pose determination for applications in aerial photogrammetry.* In: *ISPRS Annals of Photogrammetry, Remote Sensing and Spatial Information Sciences* III-3 (2016), S. 257–262

[23] AGISOFT LLC: *Agisoft Metashape User Manual - Professional Edition, Version 1.8*

[24] FERRER-GONZÁLEZ, E. ; AGÜERA-VEGA, F. ; CARVAJAL-RAMÍREZ, F. ; MARTÍNEZ-CARRICONDO, P.: *UAV Photogrammetry Accuracy Assessment for Corridor Mapping Based on the Number and Distribution of Ground Control Points.* In: *Remote Sensing* 12 (2020), No. 15, S. 2447

[25] MCDOWELL, G.: *How Does A Digital Camera Work? Technology Explained.* 2009. – URL: https://www.makeuseof.com/tag/technology-explained-how-does-a-digital-camera-work/. – Access date: 2024-04-13

[26] WANG, B.: *CCD vs CMOS: A Review of Sensor Technology.* 2024. – URL: https://www.csensor.com/ccd-vs-cmos. – Access date: 2024-02-14

[27] FROST, C.: *Sony FE 50mm f/1.8 lens review with samples (Full-frame and APS-C).* 2017. – URL: https://www.youtube.com/watch?v=yu7gvY-nQEY. – Access date: 2024-02-5

[28] GONG, X. ; BANSMER, S.: *Laser scanning applied for ice shape measurements.* In: *Cold Regions Science and Technology* 115 (2015), S. 64–76. – ISSN 0165232X

[29] HAN, Y. ; PALACIOS, J. L. ; SMITH, E. C.: *An Experimental Correlation between Rotor Test and Wind Tunnel Ice Shapes on NACA 0012 Airfoils.* In: *SAE International* (2011)

[30] REEHORST, A. ; RICHTER, G.: *New Methods and Materials for Molding and Casting Ice Formations.* In: *NASA Tech. Memo* 100126 (1987). – URL: https://ntrs.nasa.gov/api/citations/19870020037/downloads/19870020037.pdf. – Access date: 2024-04-24

[31] BROEREN, A. P. ; ADDY, H. ; LEE, S. ; MONSTERO, M.: *Validation of 3-D Ice Accretion Measurement Methodology for Experimental Aerodynamic Simulation.* In: *AIAA* (2015). – URL: https://ntrs.nasa.gov/api/citations/20150014966/downloads/20150014966.pdf. – Access date: 2024-04-24

[32] VELANDIA, J. S. ; BANSMER, S. E.: *Detailed atmospheric ice accretion surface measurement using micro-computed tomography.* In: *Atmospheric Science Letters* (2020). – URL: https://rmets.onlinelibrary.wiley.com/doi/epdf/10.1002/asl.997. – Access date: 2024-04-24

[33] LIU, Z. ; CHANG, S. ; LI, M. ; ZHAO, Y.: *A novel method for tracing and digitizing the 3d ice shape.* In: *Institute of Electrical and Electronics Engineers (IEEE)* (2011), S. 3679–3683

[34] BAGHEL, A. P. ; SOTOMAYOR-ZAKHAROV, D. ; KNOP, I. ; ORTWEIN, H. P.: *Detailed Study of Photogrammetry Technique as a Valid Ice Accretion Measurement Method.* In: *SAE International* (2023)

[35] GONG, X. ; BANSMER, S.: *3-d ice shape measurements using mid-infrared laser scanning.* In: *Optic Express* 23 (2015), S. 908–4926

[36] MCKNIGHT, R. C. ; PALKO, R. L. ; HUMES, R. L.: *In-flight Photogrammetric Measurement of Wing Ice Accretions.* In: *24th Aerospace Sciences Meeting* (1986), S. 1–9. – URL: https://ntrs.nasa.gov/api/citations/19860022090/downloads/19860022090.pdf. – Access date: 2024-04-27

[37] TECHNICAL RESEARCH CENTRE OF FINLAND: *Icing wind tunnel: Brochure.* 2020. – URL: https://www.vttresearch.com/sites/default/files/2020-06/Wind%20power_Icing_wind_tunnel.pdf. – Access date: 2024-03-06

[38] VALLEJO FARBEN: *Vallejo Model Air: 001 White, 17 ml.* 2024. – URL: https://www.vallejo-farben.de/vallejo-model-air-001-white-17-ml. – Access date: 2024-04-24

[39] SONY GROUP CORPORATION: *ILCE 6400: Specifications.* 2024. – URL: https://www.sony.com/electronics/support/e-mount-body-ilce-6000-series/ilce-6400/specifications. – Access date: 2024-04-13

[40] SONY GROUP CORPORATION: *FE 50mm F1.8: Technische Daten und Funktionen.* 2024. – URL: https://www.sony.de/electronics/kamera-objektive/sel50f18f#product_details_default. – Access date: 2024-04-13

[41] ORANGEMONKIE: *Foldio3.* 2024. – URL: https://orangemonkie.com/pages/foldio3. – Access date: 2024-04-13

[42] ORANGEMONKIE: *Foldio360 Smart Turntable.* 2024. – URL: https://orangemonkie.com/pages/foldio360-turntable. – Access date: 2024-04-13

[43] OVER, J. S. R. ; RITCHIE, A. C. ; KRANENBURG, C. J. ; BROWN, J. A. ; BUSCOMBE, D. ; NOBLE, T. ; SHERWOOD, C. R. ; WARRICK, J. A. ; WERNETTE, P. A.: *Processing coastal imagery with Agisoft Metashape Professional Edition, version 1.6—Structure from motion workflow documentation.* (2021). – URL: https://pubs.usgs.gov/of/2021/1039/ofr20211039.pdf. – Access date: 2024-02-08

[44] MILOSAVLJEVIC, N.: *Rigid Body Transform.* In: *Stanford University* (2004). – URL: https://web.stanford.edu/class/cs273/scribing/2004/class1/lect1.pdf. – Access date: 2024-03-14

[45] SPONG, M. W. ; HUTCHINSON, S. ; VIDYASAGAR, M.: *Robot modeling and control.*
      Second edition. Hoboken, NJ : Wiley, 2020. – ISBN 9781119523994

[46] DEUTSCHES INSTITUT FÜR NORMUNG: *DIN 9300-1: Begriffe, Größen und Formelze-
      ichen der Flugmechanik: Bewegung des Luftfahrzeuges gegenüber der Luft.* 1990-10

[47] TECPLOT INC.:   *Tecplot 360.*   2024. –   URL: `https://tecplot.com/products/`
      `tecplot-360/`. – Access date: 2024-04-29

[48] TSAO, J.-C.: *Further Evaluation of Swept Wing Icing Scaling with Maximum Combined
      Cross Section Ice Shape Profiles.* In: *AIAA AVIATION Forum* (2018)

[49] PYPI: *Alpha Shape Toolbox.* 2021. – URL: `https://pypi.org/project/alphashape/`.
      – Access date: 2024-04-01

[50] ROCKAFELLAR, R. T. ; WETS, R. J.-B.: *Die Grundlehren der mathematischen Wis-
      senschaften in Einzeldarstellungen.* Bd. 317: *Variational analysis.* Berlin and Heidel-
      berg : Springer, 1998. – ISBN 3-540-62772-3

[51] ISTI - CNR: *MeshLab.* 2024. – URL: `https://www.meshlab.net/`. – Access date:
      2024-04-29

[52] GERLINGER, P.: *Numerische Verbrennungssimulation: Effiziente numerische Simula-
      tion turbulenter Verbrennung: Zugl.: Stuttgart, Univ., Habil.-Schr., 2004.* Berlin and
      Heidelberg : Springer, 2005. – ISBN 978-3-540-23337-4

[53] APPLE INC.: *iPhone SE (2. Generation) - Technische Daten.* 2024. – URL: `https:`
      `//support.apple.com/de-de/111882`. – Access date: 2024-04-13

[54] VARGAS, M. ; BROUGHTON, H. ; SIMS, J. J. ; BLEEZE, B. ; GAINES, V.: *Local and
      Total Density Measurements in Ice Shapes.* In: *AIAA* (2005). – URL: `https://`
      `ntrs.nasa.gov/api/citations/20050160244/downloads/20050160244.pdf`. – Ac-
      cess date: 2024-04-09

[55] AGISOFT METASHAPE: *Online Store.* 2024. – URL: `https://www.agisoft.com/buy/`
      `online-store/`. – Access date: 2024-08-28

Eidesstattliche Erklärung

Hiermit versichere ich, die vorliegende Abschlussarbeit selbstständig und nur unter Verwendung der von mir angegebenen Quellen und Hilfsmittel verfasst zu haben. Sowohl inhaltlich als auch wörtlich entnommene Inhalte wurden als solche kenntlich gemacht. Die Arbeit hat in dieser oder vergleichbarer Form noch keinem anderem Prüfungsgremium vorgelegen.

Datum: Trondheim, 30.04.2024   Unterschrift: S. Göhring

Declaration of AI aids and -tools

Have any AI-based aids or tools been used in the creation of this report?

○ No

◉ Yes

If *yes*: please specify the aid/tool and area of use below.

Text

☑ **Spell checking.** Are parts of the text checked by:
Grammarly, Ginger, Grammarbot, LanguageTool, ProWritingAid, Sapling, Trinka.ai or similar tools?

☑ **Text-generation.** Are parts of the text generated by:
ChatGPT, GrammarlyGO, Copy.AI, WordAi, WriteSonic, Jasper, Simplified, Rytr or similar tools?

☑ **Writing assistance.** Are one or more of the report's ideas or approach suggested by:
ChatGPT, Google Bard, Bing chat, YouChat or similar tools?

If *yes*, use of text aids/tools apply to this report - please specify usage here:

Grammarly (Spell checking & grammar)
ChatGPT (Wording suggestions)

Codes and algorithms

☑ **Programming assistance.** Are parts of the codes/algorithms that i) appear directly in the report or ii) have been used to produce results such as figures, tables or numerical values been generated by: *GitHub Copilot, CodeGPT, Google Codey/Studio Bot, Replit Ghostwriter, Amazon CodeWhisperer, GPT Engineer, ChatGPT, Google Bard* eller lignende verktøy?

If *yes*, use of programming assistance aid/tools apply to this report - please specify usage here:

ChatGPT

Images and figures

☐ **Image generation.** Are one or more of the reports images/figures generated by:
Midjourney, Jasper, WriteSonic, Stability AI, Dall-E or similar tools?

If *yes*, use of image generator aids/tools apply to this report – please specify usage here:

Other AI aids or tools. Have you used other types of AI aids or -tools in the creation of this report?
If *yes*, please specify usage here:

DeepL for Translation

☑ I am familiar with NTNU's regulations: *Submitting a report generated with the assistance of AI tools and claiming the work to be partially or fully my own, is not permitted. I therefore declare that any use of AI aids or tools are explicitly stated i) directly in the report or ii) in this declaration form.*

S. Göhring

Signature/Date/Place